

A-POSTERIORI ERROR ESTIMATION AND ADAPTIVITY FOR MULTIPLE-NETWORK POROELASTICITY

E. ELISEUSSEN, M. E. ROGNES, AND T. B. THOMPSON

ABSTRACT. The multiple-network poroelasticity (MPET) equations describe deformation and pressures in an elastic medium permeated by interacting fluid networks. In this paper, we (i) place these equations in the theoretical context of coupled elliptic-parabolic problems, (ii) use this context to derive residual-based a-posteriori error estimates and indicators for fully discrete MPET solutions and (iii) evaluate the performance of these error estimators in adaptive algorithms for a set of test cases: ranging from synthetic scenarios to physiologically realistic simulations of brain mechanics.

1. INTRODUCTION

At the macroscale, the brain and other biological tissues can often be viewed as a poroelastic medium: an elastic structure permeated by one or more fluid networks. Such structures can be modeled via Biot's equations in the case of a single fluid network [Biot, 1941, 1955, Terzaghi, 1943] or by their generalization to the equations of multiple-network poroelasticity (MPET) which describe the case of two or more interacting fluid networks [Barenblatt et al., 1960, Barenblatt, 1963, Aifantis, 1980, Wilson and Aifantis, 1982, Khaled et al., 1984, Bai et al., 1993, Tully and Ventikos, 2011, Vardakis et al., 2016, Guo et al., 2018]. The computational expense associated with numerical solution of these equations over complex domains such as the human brain is substantial however. A natural question is therefore whether numerical error estimation and adaptivity can yield more accurate simulations of the MPET equations within a limited set of computational resources.

The quasi-static MPET equations read: given a domain Ω , a finite final time $T > 0$ and a set of J fluid networks, find the displacement field $u : [0, T] \times \Omega \rightarrow \mathbb{R}^d$ and pressure fields $p_1, p_2 \dots p_J : [0, T] \times \Omega \rightarrow \mathbb{R}$ such that

$$(1.1a) \quad -\operatorname{div} \sigma(u) + \sum_{j=1}^J \alpha_j \nabla p_j = f,$$

$$(1.1b) \quad \partial_t (s_j p_j + \alpha_j \operatorname{div} u) - \operatorname{div} (\kappa_j \nabla p_j) + T_j = g_j.$$

The quantity $\sigma(u) = 2\mu \varepsilon(u) + \lambda \operatorname{tr}(\varepsilon(u)) \mathbf{I}$ in (1.1a) is the elastic stress tensor and involves the displacement u , the linearized strain tensor $\varepsilon(u) = \frac{1}{2}(\nabla u + \nabla u^T)$, the $d \times d$ identity matrix \mathbf{I} and the material Lamé coefficients μ and λ . Each one of the J fluid networks is associated with a Biot-Willis coefficient α_j , a storage coefficient s_j , and a hydraulic conductivity κ_j . An interpretation of the Biot Willis and storage coefficients, in the MPET context, appears in [Bai et al., 1993, Section §3]. We use transfer terms T_j in (1.1b) of the form

$$(1.2) \quad T_j = \sum_{i=1}^J T_{ji}, \quad T_{ji} = \gamma_{ji}(p_j - p_i).$$

Date: November 29, 2021.

This project has received funding from the European Research Council (ERC) under the European Union's Horizon 2020 research and innovation programme under grant agreement 714892 and by the Research Council of Norway under the FRINATEK Young Research Talents Programme through project #250731/F20 (Waterscape). Parts of the computations were performed on resources provided by UNINETT Sigma2 - the National Infrastructure for High Performance Computing and Data Storage in Norway.

The coefficients γ_{ji} regulate the interplay between network i and network j and T_j is the total transfer out of network j (into the other networks). The transfer term vanishes when $J = 1$ and (1.1) coincides with Biot's equations for a single fluid in a poroelastic medium. We also note that the fluid (Darcy) velocity v_j in network j is defined by

$$(1.3) \quad v_j = -\kappa_j \nabla p_j.$$

Over the last decade, several authors have studied a-posteriori error estimation and adaptivity related to (1.1) in the case of $J = 1$; that is, for Biot's equations of poroelasticity. Depending on the application of interest, different formulations of Biot's equations have been used which introduce additional solution fields such as the Darcy velocity, the total pressure or the effective stress. In each case, a-posteriori methods have been developed to facilitate adaptive refinement strategies. In [Riedlbeck et al. \[2017\]](#), the authors consider the standard two-field formulation of Biot's equation in two spatial dimensions, develop an a-posteriori error analysis based on $H(\text{div})$ reconstructions of the flux and effective stress and apply the resulting estimators to construct a time-space adaptive algorithm. [Kuman et al. \[2021\]](#) used a-posteriori estimators to provide error estimates for the popular fixed-stress iterative solution scheme applied to the two-field formulation. Formulations with additional fields have also been considered for Biot's equations. The total pressure formulation of [Ricardo and Ruiz-Baier \[2016\]](#) is a locking-free, three-field formulation, ideal for a nearly-incompressible poroelastic material. A-priori estimates, and an adaptive refinement strategy, for this formulation are constructed in [Khan and Silvester \[2020\]](#) for quadrilateral and simplicial meshes. Residual-based a-posteriori error estimates have also been advanced by [Li and Zikatanov \[2019\]](#) for a lowest-order discretization of the standard Darcy-flux three-field formulation which, as shown by [Rodrigo et al. \[2018\]](#), robustly preserves convergence in the presence of vanishingly small hydraulic conductivity. Finally, [Ahmed et al. \[2019\]](#) proposed a four-field formulation, with symmetric stress and a Darcy velocity, of Biot's equations and developed a-posteriori error estimates and an adaptive refinement based on post-processed pressure and displacement fields.

The a-posteriori landscape for the more general MPET system (1.1) is considerably sparse. A-posteriori error estimates for the two-field formulation of the Barenblatt-Biot equations (corresponding to the $J = 2$ case of (1.1)) have indeed been obtained by [Nordbotten et al. \[2010\]](#). In general, though, there has been little work on the development of a-posteriori error estimators for (1.1), for formulations with any number of fields, in the case of more than one fluid network (i.e. $J > 1$). However, the recent work of [Ern and Meunier \[2009\]](#) developed an abstract framework for a-posteriori error estimators for a general class of coupled elliptic-parabolic problems.

In this manuscript, our focus is three-fold. First, we rigorously place the MPET equations in the context of coupled elliptic-parabolic problems. In particular, we consider extended spaces, bilinear forms and augmentation with a semi-inner product arising from the additional transfer terms. Second, we use this context to derive specific a-posteriori error estimates and error indicators for the space-time finite element discretizations of the multiple-network poroelasticity equations in general. In biomedical applications, two-field variational formulations are often used to numerically approximate the multiple-network poroelasticity equations [[Tully and Ventikos, 2011](#), [Vardakis et al., 2016](#)], and we therefore focus on such here. Third, we formulate a physiological modelling and simulation-targeted adaptive strategy and evaluate this strategy on a series of test cases including a clinically-motivated simulation of brain mechanics.

2. NOTATION AND PRELIMINARIES

This section provides a brief account of the notation and relevant results employed throughout the remainder of the manuscript.

2.1. Domain, boundary and meshes. It is assumed that the poroelastic domain $\Omega \subset \mathbb{R}^d$ with $d \in \{1, 2, 3\}$ is a bounded, convex domain with $\partial\Omega$ Lipschitz continuous. We consider a family of mesh discretization $\{\mathcal{T}_h\}_{h>0}$ of Ω into simplices; triangles when $d = 2$ and tetrahedra when $d = 3$. Here, $h > 0$ is a characteristic mesh size such as the maximum diameter over all simplices. Furthermore, we assume that each mesh \mathcal{T}_h in the family is quasi-uniform.

2.2. Material parameters. For simplicity, we assume that all material parameters are constant (in space), and that the following (standard) bounds are satisfied: $\mu > 0$, $2\mu + \lambda > 0$, $\kappa_j > 0$, $\alpha_j \in (0, 1]$, $s_j > 0$ for $j = 1, \dots, J$, and $\gamma_{ji} = \gamma_{ij} \geq 0$ for $i, j = 1, \dots, J$ with $\gamma_{ii} = 0$. The analysis can be extended to the case where the parameters, above, vary with sufficient regularity in space and time provided the above bounds hold uniformly. For each parameter, ξ_i or ξ_{ij} above, the minimum and maximum notation

$$\xi_{\max} = \max_i \xi_i \text{ or } \max_{ij} \xi_{ij} \quad \text{and} \quad \xi_{\min} = \min_i \xi_i \text{ or } \min_{ij} \xi_{ij},$$

will be used throughout the manuscript; the notational extension to the case of smoothly varying parameters, on a bounded domain with compact closure, is clear.

2.3. Norms and function spaces. Let f, g denote real-valued functions with domain $\Omega \subset \mathbb{R}^d$. If there exists a generic constant C with $f \leq Cg$ then we write

$$f \lesssim g.$$

The notation $\langle f, g \rangle$ signifies the usual Lebesgue inner product defined by

$$\langle f, g \rangle = \int_{\Omega} fg \, dx,$$

and $\|f\| = \langle f, f \rangle^{1/2}$ is the corresponding norm on the Hilbert space of square-integrable functions

$$L^2(\Omega) = \{f : \Omega \rightarrow \mathbb{R} \mid \|f\| < \infty\}.$$

When the context is evident in praxis the domain, Ω , is suppressed in the above expressions. Given w a positive constant, positive scalar field, or positive-definite tensor field, the symbolics

$$\langle f, g \rangle_w = \langle wf, g \rangle, \quad \|f\|_w = \langle f, f \rangle_w^{1/2},$$

refer to a w -weighted inner product and norm, respectively.

The Sobolev space $H^1(\Omega)$, often abbreviated as simply H^1 , consists of those functions $f \in L^2$ whereby $\partial_{x_j} f$ exists, in the sense of distributions, for every $j = 1, 2, \dots, d$ and $\partial_{x_j} f \in L^2$. The associated norm is given by the expression

$$\|f\|_{H^1} = \left(\|f\|^2 + \sum_{j=1}^d \|\partial_{x_j} f\|^2 \right)^{1/2}.$$

The subset $H_0^1 \subset H^1$ signifies functions with zero trace on the boundary; that is, those functions $f \in H^1$ such that $f(x) = 0$ for almost every $x \in \partial\Omega$. In addition, given a Hilbert space X with inner product $\langle \cdot, \cdot \rangle_X$, the notation $[X]^d$ refers to vectors $f = [f_1, f_2, \dots, f_d]^T$ whereby $f_j \in X$ for each $j = 1, 2, \dots, d$. The natural inner product on $[X]^d$, in which $[X]^d$ is also a Hilbert space, is then

$$\langle f, g \rangle = \sum_{j=1}^d \langle f_j, g_j \rangle_X,$$

with resulting norm

$$\|f\|_{X^d} = \left(\sum_{j=1}^d \|f_j\|_X^2 \right)^{1/2}.$$

The additional decoration of the inner product, for the case of a Hilbert space X , will be omitted when the context is clear. For X any Banach space, the notation X^* denotes the dual space, and we also write $\langle x^*, x \rangle_{X^* \times X}$ for the duality pairing. Accordingly, the operator norm on X^* is denoted

$$\|x^*\|_{X^*} = \sup_{\|x\|_X=1} |\langle x^*, x \rangle_{X^* \times X}|.$$

Unlike the inner product case, the decoration of the duality pairing bracket notation will always be made explicit and never omitted.

We also recall the canonical definition [Evans, 2010] of some useful time-dependent spaces whose codomain is also a given Hilbert space X . With X selected we consider a strongly measurable function $f : [0, T] \rightarrow X$. Then $f \in L^2(0, T; X)$ means that

$$\|f\|_{L^2(0, T; X)} = \left(\int_0^T \|f(t)\|_X^2 dt \right)^{1/2} < \infty,$$

whereas $f \in L^\infty(0, T; X)$ implies

$$\|f\|_{L^\infty(0, T; X)} = \operatorname{ess\,sup}_{0 \leq t \leq T} \|f(t)\|_X < \infty,$$

and $f \in C(0, T; X)$ means that

$$\|f\|_{C(0, T; X)} = \max_{0 \leq t \leq T} \|f(t)\|_X < \infty.$$

We now discuss those strongly measurable functions, $f : [0, T] \rightarrow X$, which possess weakly differentiability in time. The space $H^1(0, T; X)$ denotes the collection of functions, $f \in L^2(0, T; X)$, such that $\partial_t f$ exists, in the weak sense, and also resides in $L^2(0, T; X)$. This is similar to the usual definition of $H^1(\Omega)$, given above, and the norm corresponding to this space is also similar; it is given by

$$\|f\|_{H^1(0, T; X)} = \left(\int_0^T \|f(t)\|_X^2 + \|\partial_t f(t)\|_X^2 dt \right)^{1/2}.$$

Likewise, $f \in C^k(0, T; X)$ implies that f and its first k weak derivatives in time, $\partial_t^j f$ for $j = 1, 2, \dots, k$, all reside in $C(0, T; X)$.

2.4. Mesh elements and discrete operators. For a fixed h , the mesh \mathcal{T}_h is composed of simplices, denoted $T \in \mathcal{T}_h$, and faces (edges in 2D) $e \in \partial T$. Let Γ denote the complete set of faces of simplices $T \in \mathcal{T}_h$; then Γ can be written as the disjoint union

$$\Gamma = \Gamma_{int} \cup \Gamma_{bd},$$

where $e \in \Gamma_{int}$ if e is an interior edge and $e \in \Gamma_{bd}$ if e is a boundary edge.

Let f be a scalar or vector valued function and suppose e is an interior edge $e \in T_+ \cap T_-$ where T_+ and T_- are two simplices with an arbitrary but fixed choice of labeling for the pairing. We denote by n_e the outward facing normal associated to T_+ . We use an explicit jump operator defined, for $e \in \Gamma_{int}$, by

$$(2.1) \quad [f] = f_+ - f_-$$

where f_+ denotes f restricted to $e \in T_+$ and f_- denotes f restricted to $e \in T_-$. For an edge $e \in \Gamma_{bd}$ we have that there exists only one $T_+ = T \in \mathcal{T}_h$ such that $e \in \partial T$ and in this case we define

$$[f] = f_+.$$

2.5. Boundary and initial conditions. We assume homogeneous boundary conditions for the displacement and pressures; though, as in [Ern and Meunier, 2009], these conditions can easily be generalized [Showalter, 2000].

3. COUPLED ELLIPTIC-PARABOLIC PROBLEMS AS A SETTING FOR POROELASTICITY

To consider the a-posteriori error analysis of the generalized poroelasticity equations (1.1), we follow the general framework for a-posteriori error analysis for coupled elliptic-parabolic problems presented by Ern and Meunier [2009]. In Section 3.1 below, we briefly overview this general framework and its application to Biot's equations. Next, we show that (1.1) can be addressed using this general framework, also for the case where $J > 1$ under appropriate assumptions on the transfer terms $T_{m \rightarrow n}$, in Section 3.2. Based on the general framework, Ern and Meunier derive and analyze several a-posteriori error estimators. These estimators, and their corresponding extensions to the generalized poroelasticity equations, will be discussed in Section 5.

3.1. The coupled elliptic-parabolic problem framework. The setting introduced by Ern and Meunier [Ern and Meunier, 2009] for coupled elliptic-parabolic problems provides a natural setting also for generalized poroelasticity. The general coupled elliptic-parabolic problem reads as: find $(u, p) \in H^1(0, T; V_a) \times H^1(0, T; V_d)$ that satisfy (for almost every $t \in [0, T]$):

$$(3.1a) \quad a(u, v) - b(v, p) = \langle f, v \rangle_{V_a^* \times V_a}, \quad \forall v \in V_a,$$

$$(3.1b) \quad c(\partial_t p, q) + b(\partial_t u, q) + d(p, q) = \langle g, q \rangle_{V_d^* \times V_d}, \quad \forall q \in V_d.$$

The data, f and g in (1.1), are general and assumed to satisfy $f \in H^1(0, T; V_a^*)$ and $g \in H^1(0, T; V_d^*)$. The initial pressure is assumed to satisfy $p(0) \in V_d$. Moreover, it is assumed that

- (1) V_a and V_d are Hilbert spaces.
- (2) $a : V_a \times V_a \rightarrow \mathbb{R}$ and $d : V_d \times V_d \rightarrow \mathbb{R}$ are symmetric, coercive, and continuous bilinear forms, thus inducing associated inner-products and norms (denoted by $\|\cdot\|_a$ and $\|\cdot\|_d$) on their respective spaces.
- (3) There exist Hilbert spaces L_a and L_d with $V_a \subset L_a$ and $V_d \subset L_d$, where the inclusion is dense and such that $\|f\|_{L_a} \lesssim \|f\|_a$ for $f \in V_a$, and $\|g\|_{L_d} \lesssim \|g\|_d$ for $g \in V_d$.
- (4) $c : L_d \times L_d \rightarrow \mathbb{R}$ is symmetric, coercive and continuous; thereby defining an equivalent norm $\|\cdot\|_c$ on L_d .
- (5) There exists a continuous bilinear form $b : V_a \times L_d \rightarrow \mathbb{R}$ such that $|b(f, g)| \lesssim \|f\|_a \|g\|_c$ for $f \in V_a$ and $g \in L_d$.

Example 3.1. Biot's equations of poroelasticity (i.e. (1.1) for $J = 1$ fluid networks) fit the coupled elliptic-parabolic framework with

$$V_a = [H_0^1]^d, \quad L_a = [L^2]^d, \quad V_d = H_0^1, \quad L_d = L^2.$$

and

$$\begin{aligned} a(u, v) &= \langle \sigma(u), \varepsilon(v) \rangle, \\ b(u, p) &= \langle \alpha_1 p, \operatorname{div} u \rangle, \quad c(p, q) = \langle c_1 p, q \rangle, \quad d(p, q) = \langle \kappa_1 \nabla p, \nabla q \rangle, \end{aligned}$$

with the standard (vector) H_0^1 -inner product and norm on V_a and V_d , and L^2 -inner product and norm on L_a and L_d . It is readily verifiable that the general conditions described above are satisfied under these choices of spaces, norms, inner products and forms [Ern and Meunier, 2009].

3.2. Generalized poroelasticity as a coupled elliptic-parabolic problem. In this section, we derive a variational formulation of the generalized poroelasticity equations (1.1) for the case of several fluid networks (i.e. $J \geq 1$) and show how this formulation fits the general framework presented above. The extension from Biot's equations to generalized poroelasticity is natural in the sense it coincides with the original application of the general framework to Biot's equations when $J = 1$.

Now suppose that the total number of networks J is arbitrary but fixed. We define the spaces

$$(3.2) \quad V_a = [H_0^1]^d, \quad L_a = [L^2]^d, \quad V_d = [H_0^1]^J, \quad L_d = [L^2]^J.$$

We consider data such that $f \in H^1(0, T; L_a)$ and $(g_1, g_2, \dots, g_J) \in H^1(0, T; L_d)$ with given initial network pressures determined by $p(0) \in V_d$. A standard multiplication, integration and integration by parts yield the following variational formulation of (1.1): find $u \in H^1(0, T; V_a)$ and $p = (p_1, \dots, p_J) \in H^1(0, T; V_d)$ such that for a.e. $t \in (0, T]$:

$$(3.3a) \quad \langle \sigma(u), \varepsilon(v) \rangle - \sum_{j=1}^J \langle \alpha_j p_j, \operatorname{div} v \rangle = \langle f, v \rangle,$$

$$(3.3b) \quad \sum_{j=1}^J \langle \partial_t s_j p_j, q_j \rangle + \langle \partial_t \alpha_j \operatorname{div} u, q_j \rangle + \langle \kappa_j \nabla p_j, \nabla q_j \rangle + \langle T_j, q_j \rangle = \sum_{j=1}^J \langle g_j, q_j \rangle.$$

for $v \in V_a$, $q = (q_1, \dots, q_J) \in V_d$. As noted in [Ern and Meunier, 2009], (3.3a) holds up to time $t = 0$ so that u_0 is determined by the initial data $p(0)$ and initial right-hand side $f(0)$. By labeling

the forms

$$(3.4a) \quad a(u, v) = \langle \sigma(u), \varepsilon(v) \rangle,$$

$$(3.4b) \quad b(u, p) = \sum_{j=1}^J \langle \alpha_j p_j, \operatorname{div} u \rangle,$$

$$(3.4c) \quad c(p, q) = \sum_{j=1}^J \langle s_j p_j, q_j \rangle,$$

$$(3.4d) \quad d(p, q) = \sum_{j=1}^J \langle \kappa_j \nabla p_j, \nabla q_j \rangle + \langle T_j, q_j \rangle,$$

we observe that the weak formulation (3.3) of (1.1) takes the form (3.1) where T_j , in (3.4d), is given by (1.2).

We now show that the associated assumptions on these forms and spaces hold, beginning with properties of the form d in Lemma 3.2 below.

Lemma 3.2. *The form d given by (3.4d) defines an inner product over $[H_0^1(\Omega)]^J$ with associated norm*

$$(3.5) \quad \|q\|_d^2 = d(q, q) = \sum_{j=1}^J \|\nabla q_j\|_{\kappa_j}^2 + |q|_T^2, \quad \forall q \in V_d,$$

where $|\cdot|_T$ is defined by (3.7), which is such that

$$(3.6) \quad \|q\|_d \lesssim \|q\|_{H_0^1}, \quad \forall q \in [H_0^1]^J,$$

with inequality constant depending on J , κ_{\max} , γ_{\max} and Ω .

Proof. By definition (1.2) and the assumption of symmetric transfer $\gamma_{ji} = \gamma_{ij} \geq 0$, we have

$$(3.7) \quad \sum_{j=1}^J \langle T_j, q_j \rangle = \sum_{j=1}^J \sum_{i=1}^J \langle \gamma_{ji}(p_j - p_i), q_j \rangle = \frac{1}{2} \sum_{j=1}^J \sum_{i=1}^J \langle \gamma_{ji}(p_j - p_i), (q_j - q_i) \rangle.$$

Given $p, q \in V_d$, the bilinear form defined by (3.7), that is

$$\langle p, q \rangle_T = \sum_{j=1}^J \langle T_j, q_j \rangle,$$

is clearly symmetric and satisfies the requirements of a (real) semi-inner product on $L_d \times L_d$ in the sense of [Conway, 1997]. It follows that

$$(3.8) \quad |q|_T \equiv \langle q, q \rangle_T^{1/2} = \left(\frac{1}{2} \sum_{j=1}^J \sum_{i=1}^J \langle \gamma_{ji}(q_j - q_i), (q_j - q_i) \rangle \right)^{1/2}$$

defines a semi-norm on $L_d \times L_d$ and that the corresponding Cauchy-Schwarz inequality holds. Using the triangle inequality, the definition (3.7), the bounds for γ_{ji} and the Poincaré inequality, we have that

$$(3.9) \quad |q|_T \lesssim \|q\|_{[L^2]^J} \lesssim \|q\|_{[H_0^1]^J}$$

with constant depending on γ_{\max} , J , and the domain via the Poincaré constant. Under the assumption that $\kappa_{\min} > 0$, we observe that as a result d defines an inner product and norm on $[H_0^1]^J \times [H_0^1]^J$. Similarly, (3.6) holds with constant depending on κ_{\max} in addition to γ_{\max} , J , and the domain Ω . \square

Lemma 3.2 will be used in the subsequent sections. We next show that the choices of spaces (3.2) and forms (3.4) satisfy the abstract assumptions of the framework as overviewed in Section 3.1, and summarize this result in Lemma 3.3.

Lemma 3.3. *The problem (3.3), arising from the equations of generalized poroelasticity (1.1) with material parameters as in Section 2.2, posed on the spaces (3.2) with bilinear forms defined via (3.2) is a coupled elliptic-parabolic problem and satisfy the assumptions set forth in [Ern and Meunier, 2009].*

Proof. We consider each assumption in order. These are standard results, but explicitly included here for the sake of future reference.

- (1) V_a and V_d defined by (3.2) are clearly Hilbert spaces with natural Sobolev norms $\|\cdot\|_{H_0^1}$.

- (2) a is symmetric, coercive on V_a by Korn's inequality and the lower bounds on μ , $2\mu + d\lambda$, and continuous (with continuity constant depending on μ_{\max} and λ_{\max}). d is clearly symmetric by the transfer symmetry assumption and (3.7), coercive by $|\cdot|_T \geq e0$ and the assumption that $\kappa_{\min} > 0$:

$$d(q, q) \geq \sum_{j=1}^J \langle \nabla q_j, \nabla q_j \rangle_{\kappa_j} \geq \kappa_{\min} \sum_{j=1}^J \|q_j\|_{H_0^1}^2,$$

and continuous by Lemma 3.2.

- (3) The embedding of $(V_a, \|\cdot\|_a)$ into L_a follows from Poincaré's inequality and the coercivity of a over V_a and similarly for $V_d \hookrightarrow L_d$.
- (4) c is symmetric by definition, continuous over L_d with continuity constant depending on c_{\max} , and coercive with coercivity constant depending on $c_{\min} > 0$.
- (5) The form b given by (3.4b) is clearly bilinear and continuous on $V_a \times L_d$ as

$$|b(u, p)| = \left| \sum_{j=1}^J \langle p_j, \operatorname{div} u \rangle_{\alpha_j} \right| \lesssim \|u\|_{H^1} \left(\sum_{j=1}^J \|p_j\|^2 \right)^{\frac{1}{2}} = \|u\|_{H^1} \|p\|_{[L^2]^J} \lesssim \|u\|_a \|p\|_c$$

by applying Cauchy-Schwarz and Hölder's inequality, with constant depending on $\alpha_{\min} > 0$ and the coercivity constants of a and c . \square

In light of Lemma 3.3, the generalized poroelasticity system (3.3) is of coupled elliptic-parabolic type and takes the form of (3.1) with bilinear forms defined by (3.4).

Corollary 3.4. *The following energy estimates hold for almost every $t \in [0, T]$*

$$\begin{aligned} \|u(t)\|_a^2 + \sum_{j=1}^J s_j \|p_j(t)\|^2 + \sum_{j=1}^J \int_0^t \kappa_j \|\nabla p(s)\|^2 ds + \sum_{i=1}^J \sum_{j=1}^J \int_0^t \gamma_{ij} \|p_j(s) - p_i(s)\|^2 ds \\ \lesssim \left(\sup_{s \in [0, T]} \|f(s)\| + \int_0^T \|\partial_t f(s)\| ds \right)^2 + \int_0^T \|g(s)\|^2 ds + \|u_0\|_a^2 + \sum_{j=1}^J s_j \|p_0\|^2 \end{aligned}$$

Proof. The proof follows directly from Lemma 3.3, the corresponding energy estimates for coupled elliptic-parabolic systems [Ern and Meunier, 2009, Prop. 2.1] and the definition of the norms arising from the forms (3.4). Moreover, the proportionality constant in the estimates is independent of all material parameters and the number of networks. \square

Remark 3.1. The elliptic-parabolic MPET energy estimates, of Corollary 3.4, are similar to those of the total pressure formulation [Lee et al., 2019, Theorem 3.3] when the second Lamé coefficient, λ , is held constant in the latter. The primary difference is that [Lee et al., 2019] separates the estimates of u from that of the solid pressure, $\lambda \operatorname{div} u$, by including the latter term into a 'total pressure' variable. This allows for $\|u\|_1$ to be estimated directly, in [Lee et al., 2019], regardless of the value of λ used in the definition of $\|u\|_a$.

Remark 3.2. The conditions of Section 3.1, i.e. conditions (2)-(5), can place restrictions on the generalized poroelastic setting. As an example, the assumption of a vanishing storage coefficient has appeared in the literature as a modeling simplification [Lotfian and Sivaselvan, 2018, Young et al., 2014]. However, the coercivity requirement of condition (4) precludes the use of a vanishing specific storage coefficient, s_j in (3.4c), for any network number $j = 1, 2, \dots, J$. Care should be taken to ensure that any modeling simplifications produce forms that satisfy the conditions of Section 3.1 in order for the results of Corollary 3.4 and Section 4 to hold.

4. DISCRETIZATION AND A-PRIORI ERROR ESTIMATES

4.1. An Euler-Galerkin discrete scheme. We now turn to an Euler-Galerkin discretization of (1.1) in the context of such discretizations of coupled elliptic-parabolic problems in general [Ern and Meunier, 2009]. We employ an implicit Euler discretization in time and conforming finite elements in space.

We consider a family of simplicial meshes $\{\mathcal{T}_h\}_{h>0}$ with h a characteristic mesh size such as the maximal element diameter

$$h = \max \{h_K = \text{diam}(K) \mid K \in \mathcal{K}_h\}.$$

Furthermore, let $\{V_{a,h}\}_h$ and $\{V_{d,h}\}_h$ denote two families of finite dimensional subspaces of V_a and V_d , as in (3.2), respectively, defined relative to $\{\mathcal{T}_h\}_h$. For a final time $T > 0$ we let $0 = t_0 < t_1 < \dots < t_N = T$ denote a sequence of discrete times and set $\tau_n = t_n - t_{n-1}$. For functions and fields, we use the superscript n to refer values at timepoint t_n . We also utilize the discrete time differential notation δ_t where

$$(4.1) \quad \delta_t u_h^n = \tau_n^{-1} (u_h^n - u_h^{n-1}).$$

With this notation, the discrete problem is to seek $u_h^n \in V_{a,h}$ and $p_h^n = (p_{1,h}^n, p_{2,h}^n, \dots, p_{J,h}^n) \in V_{d,h}$ such that for all timesteps t_n with $n \in \{1, 2, \dots, N\}$:

$$(4.2a) \quad a(u_h^n, v_h) - b(v_h, p_h^n) = \langle f_h^n, v_h \rangle \quad \forall v_h \in V_{a,h},$$

$$(4.2b) \quad c(\delta_t p_h^n, q_h) + b(\delta_t u_h^n, q_h) + d(p_h^n, q_h) = \langle g_h^n, q_h \rangle \quad \forall q_h \in V_{d,h},$$

where the spaces and forms are defined by (3.2) and (3.4). The right-hand sides, above, express the inner product of the discrete approximations $f_h^n \in L_{a,h}$, to f and $g_h^n \in L_{d,h}$, to g , at time t_n . By Lemma 3.3 and [Ern and Meunier, 2009, Lemma 2.1], the discrete system (4.2) is well-posed.

4.2. A-priori error estimates. Now, let $V_{a,h}$ and $V_{d,h}$ be spatial discretizations arising from continuous Lagrange elements of order k_a and k_d , respectively, where $k_d = k_a - 1$; this relation on relative degree results directly from the framework hypotheses [Ern and Meunier, 2009, Section 2]. Let $\mathcal{P}_k(T)$ denote polynomials of order k on a simplex $T \in \mathcal{T}_h$. We consider the continuous Lagrange polynomials of order k_a and k_{a-1} defined by

$$(4.3) \quad V_{a,h} = \{v_h \in C^0(\bar{\Omega}) \mid v_h|_T \in \mathcal{P}_{k_a}(T) \text{ for every } T \in \mathcal{T}_h\},$$

$$(4.4) \quad V_{d,h} = [\{q_h \in C^0(\bar{\Omega}) \mid q_h|_T \in \mathcal{P}_{k_a-1}(T) \text{ for every } T \in \mathcal{T}_h\}]^J$$

as the discrete spaces for the displacement and network pressures, respectively. When $J = 1$ this choice coincides with the previous [Ern and Meunier, 2009] discretization considered for Biot's equations.

The general framework stipulates that three hypotheses [Ern and Meunier, 2009, Section 2.5], restated here for completeness, should be satisfied for the discretization.

Hypothesis 4.1. *There exists positive real numbers, denoted s_a and s_d , and subspaces, $W_a \subset V_a$ and $W_d \subset V_d$ equipped with norms $\|\cdot\|_{W_a}$ and $\|\cdot\|_{W_d}$, such that the following estimates hold independently of h*

$$(4.5) \quad \forall v \in W_a, \quad \inf_{v_h \in V_{a,h}} \|v - v_h\|_a \lesssim h^{s_a} \|v\|_{W_a},$$

$$(4.6) \quad \forall q \in W_d, \quad \inf_{q_h \in V_{d,h}} \|q - q_h\|_d \lesssim h^{s_d} \|q\|_{W_d}.$$

Hypothesis 4.2. *There exists a real number δ such that for every $r \in L_d$, the unique solution $\phi \in V_d$ for the dual problem*

$$d(q, r) = c(r, q) \quad \forall q \in V_d,$$

is such that there exists $\phi_h \in V_{d,h}$ satisfying

$$\|\phi - \phi_h\|_d \lesssim h^\delta \|r\|_c.$$

Hypothesis 4.3. $s_a = s_d + \delta$

We now state the primary result of this section.

Lemma 4.4. *The discrete two-field variational formulation of the MPET equations (4.2) with the choice of discrete spaces $V_{a,h}$ (4.3) and $V_{d,h}$ (4.4) satisfy the elliptic-parabolic framework hypotheses 4.1–4.3, above.*

Proof. Choose $s_a = k_a$ and $s_d = k_{a-1}$. Then the conditions of Hypothesis 4.1 follow, as in [Ern and Meunier, 2009], from choosing $W_a = [H_0^1 \cap H^{k_{a+1}}(\mathcal{T}_h)]^3$ and $W_d = [H_0^1 \cap H^{k_a}(\mathcal{T}_h)]^J$ where $H^k(\mathcal{T}_h)$ denotes the broken Sobolev space of order k on the mesh \mathcal{T}_h . The estimate (4.5) follows, without extension, directly from classical results in approximation theory [Ern and Guermond, 2004]; precisely as discussed in [Ern and Meunier, 2009]. Similarly, the estimate (4.6) follows from the properties of d , standard interpolation estimates [Ern and Guermond, 2004], and the product structure of V_d and $V_{d,h}$.

For hypothesis 4.2, we use the elliptic regularity, c.f. standard well posedness and interior regularity arguments in [Evans, 2010, Chp. 6], of the solution to the coupled linear diffusion-reaction equation of finding $\phi \in V_d$ such that

$$A\phi + \Gamma\phi = R \quad \text{for } R \in L_d,$$

where A is the $J \times J$ diagonal Laplacian matrix

$$(4.7) \quad \begin{pmatrix} -\Delta & 0 & \dots & 0 \\ 0 & -\Delta & \dots & 0 \\ \vdots & \ddots & \ddots & \vdots \\ 0 & 0 & 0 & -\Delta \end{pmatrix},$$

and Γ is a matrix composed of the transfer coefficients γ_{ij} : $\Gamma_{ii} = \sum_j \gamma_{ji}$, and $\Gamma_{ij} = -\gamma_{ij}$ for $j \neq i$. It follows from Lemma 3.2, and Γ symmetric and positive-semi definite, that the solution $\phi \in V_d$ to the dual problem

$$(4.8) \quad d(w, \phi) = c(R, w) = \langle R, w \rangle_{L'_d, V_d}, \quad \text{for all } w \in V_d,$$

lies in $[H^2]^J$ with $\|\phi\|_{H^2} \lesssim \|R\|_{L_d} = \|R\|_c$. Using this and standard interpolation results we have $\phi_h \in V_{d,h}$ with

$$\|\phi - \phi_h\|_d \lesssim h^\delta \|R\|_c = h^\delta \|R\|_{L_d},$$

where $\delta = 1$; exactly as in [Ern and Meunier, 2009]. Finally, with $\delta = 1$ and the choices $s_a = k_a$ and $s_d = k_a - 1$, hypothesis 4.3 also holds. \square

A-priori estimates for the Euler-Galerkin discretization (4.2) of the generalized poroelasticity equations (1.1) then follow directly from [Ern and Meunier, 2009, Theorem 3.1]. These estimates will be used in the a-posteriori analysis and are restated from [Ern and Meunier, 2009], subject to the extended spaces and forms of (3.2) and (3.4).

Corollary 4.5 (A-priori estimates for generalized poroelasticity). *Let $I_n = [t_{n-1}, t_n]$ denote the n^{th} time sub-interval of $[0, T]$ for $n = 1, 2, \dots, N$ of length $\tau_n = t_n - t_{n-1}$. Suppose the exact solution (u, p) to (3.3) satisfies $u \in C^1(0, T; W_a) \cap C^2(0, T; V_d)$ and $p \in C^1(0, T; W_d) \cap C^2(0, T; L_d)$, where W_a and W_d are given above with V_a and L_d as in (3.2). It is also assumed that the initial data satisfies*

$$\|u_0 - u_{0,h}\|_a \lesssim h^{k_a} \|u_0\|_{W_a} \quad \text{and} \quad \|p_0 - p_{0,h}\|_c \lesssim h^{k_a} \|p_0\|_{W_d}.$$

Define

$$\begin{aligned} C_1^n(u, p) &= \|\partial_t p(s)\|_{L^\infty(I_n; W_d)}^2 + \|\partial_t u(s)\|_{L^\infty(I_n; W_a)}^2, \\ C_2^n(u, p) &= \|\partial_{tt}^2 p(s)\|_{L^\infty(I_n; L_d)}^2 + \|\partial_{tt}^2 u(s)\|_{L^\infty(I_n; V_a)}^2, \\ C^n(f, g) &= \|f^n - f_h^n\|_a^2 + \tau_n \|g^n - g_h^n\|_d^2, \\ C(u_0, p_0) &= \|u_0\|_{W_a}^2 + \|p_0\|_{W_d}^2. \end{aligned}$$

Setting, for simplicity, $s = k_a$ then $s = k_a + 1$, by the selection of the discrete spaces, and we have that for each $n \in \{1, 2, \dots, N\}$

$$(4.9) \quad \begin{aligned} \|u^n - u_h^n\|_a^2 + \|p^n - p_h^n\|_c^2 &\lesssim h^{2s} C(u_0, p_0) + \sum_{m=1}^n C^m(f, g) + \sum_{m=1}^n \tau_m h^{2s} C_1^m(u, p) \\ &\quad + \sum_{m=1}^n \tau_m^3 C_2^m(u, p) + h^{2s} (\|u^n\|_{W_a}^2 + \|p^n\|_{W_d}^2), \end{aligned}$$

and

$$(4.10) \quad \begin{aligned} \sum_{m=1}^n \tau_m \|p^m - p_h^m\|_d^2 &\lesssim h^{2s} C(u_0, p_0) + \sum_{m=1}^n C^m(f, g) + \sum_{m=1}^n \tau_m h^{2s} C_1^m(u, p) \\ &+ \sum_{m=1}^n \tau_m^3 C_2^m(u, p) + \sum_{m=1}^n \tau_m h^{2s-1} \|p^m\|_{W_d}^2. \end{aligned}$$

5. A-POSTERIORI ERROR ESTIMATION FOR GENERALIZED POROELASTICITY

We now turn to discuss the implications to a-posteriori error estimates for generalized poroelasticity as viewed through the lens of the coupled elliptic-parabolic problem framework. Our focus is to derive, apply and evaluate residual-based error estimators and indicators in the context of generalized poroelasticity. We will therefore present an explicit account of abstractly defined quantities presented in [Ern and Meunier, 2009, Sec. 4.1], including e.g. the Galerkin residuals, applied in our context.

5.1. Time interpolation. We first introduce some additional notation for time interpolation (in line with [Ern and Meunier, 2009, Sec. 4.1]), and rewrite (4.2) in terms of the new notation. We let $u_{h\tau}$ denote the continuous and piecewise linear function in time, $u_{h\tau} \in H^1(0, T; V_{a,h})$ such that $u_{h\tau}(t_n) = u_h^n$. Similarly $(p_{1h\tau}, p_{2,h\tau}, \dots, p_{J,h\tau}) = p_{h\tau}$ is defined by $p_{h\tau}(t_n) = p_h^n$ and extended linearly in time. As a result, $\partial_t u_{h\tau}$, $\partial_t p_{h\tau}$ are defined for almost every $t \in (0, T)$. We also define the corresponding continuous, piecewise linear in time variants of the data, $f_{h\tau}$ and $g_{h\tau}$, by the same approach; i.e. $f_{h\tau}(t_n) = f_h^n$ and $g_{h\tau}(t_n) = g_h^n$.

Before rephrasing (4.2) using the time-interpolated variables we define piecewise constant functions in time for the pressure and right-hand side data. These are defined as $\pi^0 p_{h\tau} = p_h^n$ and $\pi^0 g_{h\tau} = g_h^n$ on $I_n = (t_{n-1}, t_n)$. Using the above notation, the discrete scheme for almost every $t \in (0, T)$ becomes

$$(5.1a) \quad a(u_{h\tau}, v_h) - b(v_h, p_{h\tau}) = \langle f_{h\tau}, v_h \rangle, \quad \forall v \in V_{a,h},$$

$$(5.1b) \quad c(\partial_t p_{h\tau}, q_h) + b(\partial_t u_{h\tau}, q_h) + d(\pi^0 p_{h\tau}, q_h) = \langle \pi^0 g_{h\tau}, q_h \rangle, \quad \forall q_h \in V_d.$$

Remark 5.1. Using the linear time interpolations defined above, such as $u_{h\tau}$ or $p_{h\tau}$, we have the following identity

$$\partial_t u_{h\tau} = \delta u_h^n \quad \text{for all } t \in I_n = (t_{n-1}, t_n),$$

so that the left-hand sides of and (4.2b) and (5.1b) are identical. However, as noted in [Ern and Meunier, 2009], the interpolants of the data, $f_{h\tau}$ and $g_{h\tau}$, are continuous and facilitate the definition of the continuous-time residuals (5.2) and (5.3).

5.2. Galerkin residuals. The Galerkin residuals [Ern and Meunier, 2009, Section 4.1] are functions of time whose co-domain lies in the dual of either V_a or V_d . More specifically, the residuals are continuous, piecewise-affine functions $\mathcal{G}_a : [0, T] \rightarrow V_a^*$ and $\mathcal{G}_d : [0, T] \rightarrow V_d^*$. In our context, of generalized poroelasticity, the Galerkin residual \mathcal{G}_a is, given any $v \in V_a$, defined by the relation

$$(5.2) \quad \langle \mathcal{G}_a, v \rangle \equiv \langle f_{h\tau}, v \rangle - a(u_{h\tau}, v) + b(v, p_{h\tau}) = \langle f_{h\tau}, v \rangle - a(u_{h\tau}, v) + \sum_{j=1}^J \langle p_{j,h\tau}, \operatorname{div} v \rangle_{\alpha_j}.$$

Similarly, \mathcal{G}_d is, given any $q = (q_1, q_2, \dots, q_J) \in V_d$, defined by the relation

$$(5.3) \quad \begin{aligned} \langle \mathcal{G}_d, q \rangle &\equiv \langle \pi^0 g, q \rangle - c(\partial_t p_{h\tau}, q) - b(\partial_t u_{h\tau}, q) - d(\pi^0 p_{h\tau}, q) \\ &= \sum_{j=1}^J \langle \pi^0 g_{j,h\tau}, q_j \rangle - \sum_{j=1}^J \langle s_j \partial_t p_{j,h\tau}, q_j \rangle - \sum_{j=1}^J \langle \alpha_j \partial_t \operatorname{div} u_{h\tau}, q_j \rangle \\ &\quad - \sum_{j=1}^J \langle \kappa_j \nabla p_j, \nabla q_j \rangle + \frac{1}{2} \sum_{j=1}^J \sum_{i=1}^J \langle \gamma_{ij} (p_{j,h\tau} - p_{i,h\tau}), (q_j - q_i) \rangle, \end{aligned}$$

Again, we note that (5.2) and (5.3) generalize the corresponding [Ern and Meunier, 2009, Sec. 4.1] residuals for the case of single-network poroelasticity studied therein.

5.3. Data, space and time estimators. The general coupled elliptic-parabolic problem framework gives a posteriori error estimates, and in particular so-called data, space and time estimators for the discrete solutions. In our context of generalized poroelasticity, these can be expressed explicitly as follows. We have terms for the data f and g given by

$$\mathcal{E}(f, g) = \|g - \pi^0 g_{h\tau}\|_{L^2(0, T; V_a^*)}^2 + (\|f - f_{h\tau}\|_{L^\infty(0, T; V_a^*)} + \|\partial_t(f - f_{h\tau})\|_{L^1(0, T; V_a^*)})^2,$$

and the framework data, space and time estimators are defined, respectively, as

$$(5.4) \quad \mathcal{E}_{\text{data}} = \|u_0 - u_{0h}\|_a^2 + \|p_0 - p_{0h}\|_c^2 + \mathcal{E}(f, g),$$

$$(5.5) \quad \mathcal{E}_{\text{space}} = \|\mathcal{G}_d\|_{L^2(0, T; V_d^*)}^2 + (\|\mathcal{G}_a\|_{L^\infty(0, T; V_a^*)} + \|\partial_t \mathcal{G}_a\|_{L^1(0, T; V_a^*)})^2,$$

$$(5.6) \quad \mathcal{E}_{\text{time}} = \frac{1}{3} \sum_{m=1}^N \tau_m \|p_h^m - p_h^{n-1}\|_d^2, \quad m \in \{0, 1, 2, \dots, N\},$$

where we recall that the norms are now defined according to the extended generalized poroelasticity spaces (3.2) and forms (3.4). We immediately have the following a-posteriori error estimate for the general MPET equations:

Proposition 5.1. *For every time t_n , with $n \in \{1, 2, \dots, N\}$, the following inequality holds*

$$(5.7) \quad \|u - u_{h\tau}\|_{L^\infty(0, t_n; V_a)}^2 + \|p - p_{h\tau}\|_{L^\infty(0, t_n; L_d)}^2 + \|p - p_{h\tau}\|_{L^2(0, t_n; V_d)}^2$$

$$(5.8) \quad + \|p - \pi^0 p_{h\tau}\|_{L^2(0, t_n; V_d)}^2 \lesssim \mathcal{E}_{\text{data}} + \mathcal{E}_{\text{space}} + \mathcal{E}_{\text{time}}$$

Proof. The proof follows from [Ern and Meunier, 2009, Thm. 4.1] and the arguments of Section 3.2. \square

5.4. Element and edge residuals. In this section we state the definition of the element and edge residuals (c.f. [Ern and Meunier, 2009, Sec. 4.1]) adapted to generalized poroelasticity. We then define from these residuals a set of a-posteriori error indicators. These indicators can be used to bound the Galerkin residuals defined in Section 5.2. The a-posteriori error indicators defined in this section will be used to carry out adaptive refinement for the numerical studies in Section 6.

5.4.1. Element and edge residuals for the momentum equation. The residuals associated with the displacement are derived from the Galerkin residual (5.2). We give them explicitly here for the sake of clarity and to facilitate implementation. For $v \in V_a$ and at time t_n , with $n \in \{1, 2, \dots, N\}$, we have

$$\langle \mathcal{G}_a^n, v \rangle = \sum_{K \in \mathcal{T}_h} \left(\langle f_{h\tau}^m, v \rangle_K - \langle \sigma(u_{h\tau}^m), \epsilon(v) \rangle_K + \sum_{j=1}^J \langle \alpha_j p_{j, h\tau}^m, \text{div } v \rangle_K \right),$$

where the notation $\langle f, g \rangle_K = \int_K f g \, dx$ denotes local integration over a simplex $K \in \mathcal{T}_h$ and we have used that $u_{h\tau}^n = u_h^n$ and $p_{j, h\tau}^n = p_{j, h}^n$ for every $n \in \{1, 2, \dots, n\}$. Integrating the above by parts over each $K \in \mathcal{T}_h$ gives

$$(5.9) \quad \langle \mathcal{G}_a^n, v \rangle = \sum_{K \in \mathcal{T}_h} \langle R_{uh, K}^n, v \rangle_K + \sum_{e \in \Gamma_{\text{int}}} \langle J_{uh, e}^n, v \rangle_e,$$

where Γ_{int} denotes the set of interior edges, $\langle f, g \rangle_e$ denotes integration over the edge e and where

$$(5.10) \quad R_{uh, K}^n = f_h^n|_K + \text{div } \sigma(u_h^n)|_K - \sum_{j=1}^J \alpha_j \nabla p_{j, h}^n|_K,$$

where the additional subscript denotes the restriction K . To define the term J_{uh}^n above we use the standard notation, of (2.1), and define

$$(5.11) \quad J_{uh, e}^n = -[\sigma(u_h^n)]_e n_e,$$

where e is an edge and n_e is the fixed choice of outward facing normal to that edge. The corresponding time-shifted local residual and jump operators are then

$$(5.12) \quad \delta_t R_{uh, K}^n = \tau_n^{-1} (R_{uh, K}^n - R_{uh, K}^{n-1}), \quad \delta_t J_{uh, e}^n = \tau_n^{-1} (J_{uh, e}^n - J_{uh, e}^{n-1}).$$

To close, we note that the conditions in [Ern and Meunier, 2009] on the jump operator, $J_{uh,e}$ above, are general and other choices satisfying the abstract requirements can be used if desired.

5.4.2. Element and edge residuals for the mass conservation equation. The residuals associated with the network pressures are derived from the Galerkin residual \mathcal{G}_d (5.3). Integrating the diffusion terms by parts, over $T \in \mathcal{T}_h$, gives

$$(5.13) \quad \langle \mathcal{G}_d, q \rangle = \sum_{K \in \mathcal{T}_h} \langle R_{ph,K}^n, q \rangle_K + \sum_{e \in \Gamma_{int}} \langle J_{ph,e}^n, q \rangle_e.$$

In the context of the extended multiple-network poroelasticity framework the strong form of the mass conservation residual, $R_{ph,K}^n \in L_d$ of (5.13), has a j^{th} component, for $j \in \{1, 2, \dots, J\}$, with

$$(5.14) \quad \{R_{ph,K}^n\}_j = g_{j,h|K}^n - s_j \delta_t p_{j,h|K}^n - \alpha_j (\operatorname{div} \delta_t u_h^n)_K + (\operatorname{div} \kappa_j \nabla p_{j,h}^n)_K - T_{j,h|K},$$

recalling that T_j is given by (1.2), and $T_{j,h}$ is its discrete analogue. In (5.14), we have also used that $\partial_t p_{j,h\tau}^n = \delta_t p_{j,h}^n = \tau_m^{-1}(p_{j,h}^n - p_{j,h}^{n-1})$, $\partial_t u_{h,\tau}^n = \delta_t u_h^n$, $p_{j,h\tau}^n = p_{j,h}^n$ and $u_{j,h\tau}^n = u_{j,h}^n$. The corresponding jump term $J_{ph,e}^n$ for $e \in \Gamma_{int}$ has j^{th} component

$$(5.15) \quad \{J_{ph,e}^n\}_j = -[\kappa_j \nabla p_{j,h}^n]_e \cdot n_e,$$

and we once more remark that other jump operators satisfying the abstract conditions in [Ern and Meunier, 2009] can also be considered. We also have the analogous time-shifted versions of the above, $\delta_t R_{ph,K}^n$ and $\delta_t J_{ph,K}^n$, just as in (5.12).

5.5. Error indicators in space and time. We now define the element-wise error indicators; these indicators will inform the construction of the a-posteriori error indicators of Section 5.6. In turn, these indicators will form the foundation of the adaptive refinement strategy of section 7. Specifically, we define element-wise indicators denoted $\eta_{u,K}^n$ and $\eta_{p,K}^n$ such that the following equalities hold for all $v \in V_a$ and $q \in V_d$

$$(5.16) \quad \langle \mathcal{G}_a^n, v \rangle = \sum_{K \in \mathcal{T}_h} \langle \eta_{u,K}^n, v \rangle, \quad \langle \mathcal{G}_d^n, q \rangle = \sum_{K \in \mathcal{T}_h} \langle \eta_{p,K}^n, q \rangle.$$

First, we define the following local error indicator associated with the momentum equation:

$$(5.17) \quad \begin{aligned} \eta_{u,K}^n &= h_K^2 \|R_{uh,K}\|_K^2 + h_K \sum_{e \in \partial K} \|J_{uh,e}^n\|_e \\ &= h_K^2 \|f_h^n + \operatorname{div} \sigma(u_h^n) - \sum_{j=1}^J \alpha_j \nabla p_{j,h}^n\|_K^2 + h_K \sum_{e \in \partial K} \|[\sigma(u_h^n)]_e \cdot n_e\|_e^2, \end{aligned}$$

where the norms $\|\cdot\|_K$ and $\|\cdot\|_e$ represent the usual L^2 , or d-dimensional L^2 , norm over a simplex, K , and edge, e , respectively. Likewise, the local error indicators associated with the mass conservation equations are

$$(5.18) \quad \begin{aligned} \eta_{p,T}^n &= h_K^2 \|R_{ph,K}^n\|_K^2 + h_K \sum_{e \in \partial K} \|J_{ph,e}^n\|_e \\ &= h_K^2 \sum_{j=1}^J \|g_{j,h}^n - s_j \delta_t p_{j,h}^n - \alpha_j \operatorname{div} \delta_t u_h^n + k_j \Delta p_{j,h}^n - \frac{1}{2} \sum_{i=1}^J \gamma_{ij} (p_{j,h}^n - p_{i,h}^n)\|_K^2 \\ &\quad + h_K \sum_{e \in \partial K} \left\| \sum_{j=1}^J [k_j \nabla p_{j,h}^n]_e \cdot n_e \right\|_e \end{aligned}$$

Similar to (5.12) we will use the time-shifted version of the local spatial error indicator for the momentum equation. This expression is given by

$$\eta_{u,K}^n(\delta_t) = h_K^2 \|\delta_t R_{uh,K}\|_K^2 + h_K \sum_{e \in \partial K} \|\delta_t J_{uh,e}\|_e^2,$$

where the right-hand is analogous to that of (5.17) by taking the time-shift of the expressions appearing inside the norm. With the local indicators in hand we immediately have the global indicators and their time-shifted version given by

$$(5.19) \quad \eta_u^n = \sum_{K \in \mathcal{T}_h} \eta_{u,K}^n, \quad \eta_p^n = \sum_{K \in \mathcal{T}_h} \eta_{p,K}^n, \quad \eta_u^n(\delta_t) = \sum_{K \in \mathcal{T}_h} \eta_{u,K}^n(\delta_t)$$

In Section 7 we will use the above expressions to define the a-posteriori error indicators informing a simple adaptive refinement strategy for the numerical simulations of Section 6.

5.6. A-posteriori error estimators. We close this section by defining the final a-posteriori error estimators:

$$(5.20) \quad \begin{aligned} \eta_1 &= \left(\sum_{n=1}^N \tau_n \eta_p^n \right)^{\frac{1}{2}}, \quad \eta_2 = \sup_{0 \leq n \leq N} (\eta_u^n)^{\frac{1}{2}}, \\ \eta_3 &= \sum_{n=1}^N \tau_n (\eta_u^n(\delta_t))^{\frac{1}{2}}, \quad \eta_4 = \left(\sum_{n=1}^N \tau_n \|p_h^n - p_h^{n-1}\|_d^2 \right)^{\frac{1}{2}} \end{aligned}$$

The summed term $\|p_h^n - p_h^{n-1}\|_d^2$, in η_4 above, can be expanded using the definition of (3.4d) as

$$\|p_h^n - p_h^{n-1}\|_d^2 = \sum_{j=1}^J \kappa_j \|\nabla (p_{j,h}^n - p_{j,h}^{n-1})\|_{L^2}^2 + \frac{1}{2} \sum_{j=1}^J \sum_{i=1}^J \gamma_{ij} \|(p_{j,h}^n - p_{i,h}^n) - (p_{j,h}^{n-1} - p_{i,h}^{n-1})\|_{L^2}^2.$$

Finally, a bound on the MPET discretization errors in terms of the a-posteriori error estimators follows:

Proposition 5.2. *For each time t_n , $n \in \{0, 1, \dots, N\}$, the following inequality for the discretization error holds*

$$\begin{aligned} \|u - u_{h\tau}\|_{L^\infty(0,t_n;V_a)} + \|p - p_{h\tau}\|_{L^\infty(0,t_n;L_d)} + \|p - p_{h\tau}\|_{L^2(0,t_n;V_d)} + \|p - \pi^0 p_{h\tau}\|_{L^2(0,t_n;V_d)} \\ \lesssim \eta_1 + \eta_2 + \eta_3 + \eta_4 + \mathcal{E}_{h0}(u_0, p_0) + \mathcal{E}_h(f, g) \end{aligned}$$

where $\mathcal{E}_{h0}(u_0, p_0)$ and $\mathcal{E}_h(f, g)$ are determined by the fidelity in the approximation of the initial data and source terms, respectively, as

$$\begin{aligned} \mathcal{E}_{h0}(u_0, p_0) &= \|u_0 - u_{h0}\|_a + \|p_0 - p_{0h}\|_c, \\ \mathcal{E}_h(f, g) &= \|g - \pi^0 g_{h\tau}\|_{L^2(0,T;V_d)} + \|f - f_{h\tau}\|_{L^\infty(0,T;V_a)} + \|\partial_t(f - f_{h\tau})\|_{L^1(0,T;V_a)}. \end{aligned}$$

Proof. The above follows from the results of [Ern and Meunier, 2009, Thm. 4.1, Prop. 4.1, Thm 4.2] applied in the context of generalized poroelasticity in light of the results of Section 3. \square

Remark 5.2. The framework result [Ern and Meunier, 2009, Prop. 4.2] is stronger than the re-statement given above. We have stated only the left-hand side quantities of primary concern for computations here.

6. NUMERICAL CONVERGENCE AND ACCURACY OF ERROR ESTIMATORS

To examine the accuracy of the computed error estimators and resulting error estimate, we first study an idealized test case with a manufactured smooth solution over uniform meshes. We will consider adaptive algorithms and meshes in the subsequent sections. All numerical experiments were implemented using the FEniCS Project finite element software [Alnæs et al., 2015].

Let $\Omega = [0, 1]^2$ with coordinates $(x, y) \in \Omega$, and let $T = 0.4$. We consider the case of three fluid networks ($J = 3$), first with $\mu = 1.0$, $\lambda = 10.0$, $\alpha_j = 0.5$, $s_j = 1.0$, $\kappa_j = 1.0$, for $j = 1, 2, 3$ and

(A) $\ u - u_{h\tau}\ _{L^\infty(0,T;(H_0^1)^d)}$						
N/dt	τ_0	$\tau_0/2$	$\tau_0/4$	$\tau_0/8$	$\tau_0/16$	Rate (h)
4	1.82×10^{-2}	1.82×10^{-2}	1.82×10^{-2}	1.82×10^{-2}	1.82×10^{-2}	1.98
8	4.71×10^{-3}	4.64×10^{-3}	4.62×10^{-3}	4.61×10^{-3}	4.61×10^{-3}	
16	1.44×10^{-3}	1.24×10^{-3}	1.18×10^{-3}	1.16×10^{-3}	1.16×10^{-3}	
32	8.51×10^{-4}	5.29×10^{-4}	3.63×10^{-4}	3.10×10^{-4}	2.96×10^{-4}	
64	7.86×10^{-4}	4.50×10^{-4}	2.40×10^{-4}	1.36×10^{-4}	9.07×10^{-5}	
Rate (τ)	0.81		0.90	0.82	0.59	1.77
(B) $\ p - p_{h\tau}\ _{L^\infty(0,T;(L^2)^J)}$						
N/dt	τ_0	$\tau_0/2$	$\tau_0/4$	$\tau_0/8$	$\tau_0/16$	Rate (h)
4	8.69×10^{-2}	8.93×10^{-2}	8.66×10^{-2}	8.52×10^{-2}	8.46×10^{-2}	1.84
8	3.97×10^{-2}	3.29×10^{-2}	2.73×10^{-2}	2.47×10^{-2}	2.36×10^{-2}	
16	3.06×10^{-2}	1.97×10^{-2}	1.23×10^{-2}	8.74×10^{-3}	7.10×10^{-3}	
32	2.89×10^{-2}	1.69×10^{-2}	9.13×10^{-3}	5.14×10^{-3}	3.16×10^{-3}	
64	2.86×10^{-2}	1.63×10^{-2}	8.46×10^{-3}	4.39×10^{-3}	2.33×10^{-3}	
Rate (τ)	0.81		0.95	0.95	0.91	1.14
(C) $\ p - p_{h\tau}\ _{L^2(0,T;(H_0^1)^J)}$						
N/dt	τ_0	$\tau_0/2$	$\tau_0/4$	$\tau_0/8$	$\tau_0/16$	Rate (h)
4	4.42×10^{-1}	5.26×10^{-1}	5.39×10^{-1}	5.41×10^{-1}	5.41×10^{-1}	0.96
8	2.37×10^{-1}	2.73×10^{-1}	2.77×10^{-1}	2.78×10^{-1}	2.78×10^{-1}	
16	1.38×10^{-1}	1.45×10^{-1}	1.42×10^{-1}	1.40×10^{-1}	1.40×10^{-1}	
32	9.81×10^{-2}	8.54×10^{-2}	7.49×10^{-2}	7.13×10^{-2}	7.03×10^{-2}	
64	8.53×10^{-2}	6.23×10^{-2}	4.46×10^{-2}	3.77×10^{-2}	3.57×10^{-2}	
Rate (τ)	0.45		0.48	0.24	0.08	1.00
(D) $\ p - \pi^0 p_{h\tau}\ _{L^2(0,T;(H_0^1)^J)}$						
N/dt	τ_0	$\tau_0/2$	$\tau_0/4$	$\tau_0/8$	$\tau_0/16$	Rate (h)
4	9.41×10^{-1}	6.94×10^{-1}	6.03×10^{-1}	5.67×10^{-1}	5.53×10^{-1}	0.95
8	7.89×10^{-1}	4.73×10^{-1}	3.49×10^{-1}	3.02×10^{-1}	2.87×10^{-1}	
16	7.44×10^{-1}	3.94×10^{-1}	2.40×10^{-1}	1.74×10^{-1}	1.50×10^{-1}	
32	7.32×10^{-1}	3.71×10^{-1}	2.03×10^{-1}	1.21×10^{-1}	8.66×10^{-2}	
64	7.29×10^{-1}	3.65×10^{-1}	1.93×10^{-1}	1.04×10^{-1}	6.09×10^{-2}	
Rate (τ)	1.00		0.92	0.89	0.77	0.99

TABLE 1. Displacement and pressure approximation errors (in different norms) and their rates of convergence for the smooth 3-network test case under uniform refinement in space (horizontal) and time (horizontal). $T = 0.4$, $\tau_0 = T/2$. Rate (τ) is the rate for the finest mesh, under time step refinement. Rate (h) is the rate for the finest time step, under mesh refinement. The diagonal rate (in bold) is the final space-time (diagonal) rate.

$\gamma_{12} = \gamma_{23} = \gamma_{13} = 1.0$. We define the following smooth solutions to (1.1):

$$\begin{aligned}
u(x, y) &= (0.1 \cos(\pi x) \sin(\pi y) \sin(\pi t), 0.1 \sin(\pi x) \cos(\pi y) \sin(\pi t)), \\
p_1(x, y) &= \sin(\pi x) \cos(\pi y) \sin(2\pi t), \\
p_2(x, y) &= \cos(\pi x) \sin(\pi y) \sin(\pi t), \\
p_3(x, y) &= \sin(\pi x) \sin(\pi y) t,
\end{aligned}$$

(A) η_1						
N/dt	τ_0	$\tau_0/2$	$\tau_0/4$	$\tau_0/8$	$\tau_0/16$	Rate (h)
4	3.30	3.19	3.13	3.09	3.08	
8	1.73	1.67	1.64	1.63	1.62	0.93
16	8.80×10^{-1}	8.52×10^{-1}	8.37×10^{-1}	8.29×10^{-1}	8.25×10^{-1}	0.97
32	4.43×10^{-1}	4.29×10^{-1}	4.22×10^{-1}	4.18×10^{-1}	4.16×10^{-1}	0.99
64	2.22×10^{-1}	2.15×10^{-1}	2.12×10^{-1}	2.10×10^{-1}	2.09×10^{-1}	1.00
Rate (τ)		0.05	0.03	0.01	0.01	1.00
(B) η_2						
N/dt	τ_0	$\tau_0/2$	$\tau_0/4$	$\tau_0/8$	$\tau_0/16$	Rate (h)
4	1.76	1.76	1.76	1.76	1.76	
8	4.51×10^{-1}	4.51×10^{-1}	4.51×10^{-1}	4.51×10^{-1}	4.51×10^{-1}	1.97
16	1.14×10^{-1}	1.14×10^{-1}	1.14×10^{-1}	1.14×10^{-1}	1.14×10^{-1}	1.99
32	2.84×10^{-2}	2.84×10^{-2}	2.84×10^{-2}	2.84×10^{-2}	2.84×10^{-2}	2.00
64	7.12×10^{-3}	7.12×10^{-3}	7.12×10^{-3}	7.12×10^{-3}	7.12×10^{-3}	2.00
Rate (τ)		-0.00	-0.00	-0.00	-0.00	2.00
(C) η_3						
N/dt	τ_0	$\tau_0/2$	$\tau_0/4$	$\tau_0/8$	$\tau_0/16$	Rate (h)
4	1.76	1.77	1.77	1.77	1.77	
8	4.51×10^{-1}	4.52×10^{-1}	4.52×10^{-1}	4.52×10^{-1}	4.52×10^{-1}	1.97
16	1.14×10^{-1}	1.14×10^{-1}	1.14×10^{-1}	1.14×10^{-1}	1.14×10^{-1}	1.99
32	2.85×10^{-2}	2.85×10^{-2}	2.85×10^{-2}	2.85×10^{-2}	2.85×10^{-2}	2.00
64	7.12×10^{-3}	7.13×10^{-3}	7.13×10^{-3}	7.13×10^{-3}	7.13×10^{-3}	2.00
Rate (τ)		-0.00	-0.00	-0.00	-0.00	2.00
(D) η_4						
N/dt	τ_0	$\tau_0/2$	$\tau_0/4$	$\tau_0/8$	$\tau_0/16$	Rate (h)
4	1.25	6.65×10^{-1}	3.39×10^{-1}	1.70×10^{-1}	8.54×10^{-2}	
8	1.28	6.81×10^{-1}	3.47×10^{-1}	1.75×10^{-1}	8.76×10^{-2}	-0.04
16	1.29	6.85×10^{-1}	3.49×10^{-1}	1.76×10^{-1}	8.81×10^{-2}	-0.01
32	1.29	6.86×10^{-1}	3.50×10^{-1}	1.76×10^{-1}	8.83×10^{-2}	-0.0
64	1.29	6.86×10^{-1}	3.50×10^{-1}	1.76×10^{-1}	8.83×10^{-2}	-0.0
Rate (τ)		0.91	0.97	0.99	1.00	1.00
(E) I_{eff}						
N/dt	τ_0	$\tau_0/2$	$\tau_0/4$	$\tau_0/8$	$\tau_0/16$	
4	5.42	5.56	5.61	5.61	5.59	
8	3.65	4.16	4.39	4.44	4.40	
16	2.62	3.15	3.58	3.80	3.82	
32	2.08	2.47	2.88	3.29	3.50	
64	1.81	2.06	2.34	2.74	3.14	

TABLE 2. Error estimators $\eta_1, \eta_2, \eta_3, \eta_4$ and their rates of convergence, and efficiency indices I_{eff} for the smooth 3-network test case under uniform refinement in space (horizontal) and time (horizontal). $T = 0.4$, $\tau_0 = T/2$. Rate (τ) is the rate for the finest mesh, under time step refinement. Rate (h) is the rate for the finest time step, under mesh refinement. The diagonal rate (in bold) is the final space-time (diagonal) rate.

with compatible Dirichlet boundary conditions, initial conditions and induced force and source functions f and g_j for $j = 1, 2, 3$.

We approximate the solutions using Taylor–Hood type elements relative to given families of meshes; i.e. continuous piecewise quadratic vector fields for the displacement and continuous piecewise linears for each pressure. The exact solutions were approximated using continuous piecewise cubic finite element spaces in the numerical computations.

6.1. Convergence and accuracy under uniform refinement. We first consider the convergence of the numerical solutions, their approximation errors and error estimators $\eta_1, \eta_2, \eta_3, \eta_4$ under uniform refinement in space and time. We define the meshes by dividing the domain into $N \times N$ squares and dividing each subsquare by the diagonal. The errors and convergence rates for the displacement and pressure approximations, measured in natural Bochner norms, are listed in Table 1. We observe that both the spatial and the temporal discretization contributes to the errors, and that all variables converges at at least first order in space and time - as expected with the implicit Euler scheme. For coarse meshes, we observe that the displacement converges at the optimal second order under mesh refinement (Table 1a).

We next consider the convergence and accuracy of the error estimators $\eta_1, \eta_2, \eta_3, \eta_4$ for the same set of discretizations (Table 2). We observe that each error estimator converge at at least first order in space-time, with η_2 and η_3 converging at second order in space and η_4 converging at first order in time.

We also define the efficiency index I_{eff} with respect to the Bochner norms used for the evaluation of the approximation error:

$$(6.1) \quad I_{\text{eff}} = \frac{\eta}{E},$$

where

$$\eta \equiv \eta_1 + \eta_2 + \eta_3 + \eta_4$$

$$E \equiv \|u - u_{h\tau}\|_{L^\infty(0,T;H_0^1)} + \|p - p_{h\tau}\|_{L^\infty(0,T;L^2)} + \|p - p_{h\tau}\|_{L^2(0,T;H_0^1)} + \|p - \pi^0 p_{h\tau}\|_{L^2(0,T;H_0^1)}.$$

Note that we use the natural norms here to investigate the practical quality and efficiency of the approximations and estimators rather than in terms of the parameter-weighted norms appearing in the theoretical bound (Proposition 5.2). For this test case, we find efficiency indices between 1.8 and 5.7, with little variation in the efficiency index between time steps for coarse meshes, and efficiency indices closer to 1 for finer meshes.

6.2. Variations in material parameters. We also study how variations in the material parameters affect the effectivity of the error estimates, again measured in terms of the effectivity index (6.1) with respect to the natural Bochner norms. The effectivity index I_{eff} for ~ 550 permutations of material parameters in the smooth 3-network test case are shown in Figure 1, including increased stiffnesses E , reduced compressibilities ν , lower transfer γ , lower hydraulic conductances κ , and lower specific storage coefficients s . We observe that the effectivity index increases with increasing ν and E , in agreement with theoretical expectations of a uniform bound on the error measured in the a -norm (which depends on ν and E). The efficiency indices are moderately reduced with reduced κ , but remain above 0.2 for the range conductances tested. The efficiency index varies but little with the transfer coefficients γ , but we note more variation with γ for low conductances κ . Finally, α and s seem to have less of an effect on the effectivity index.

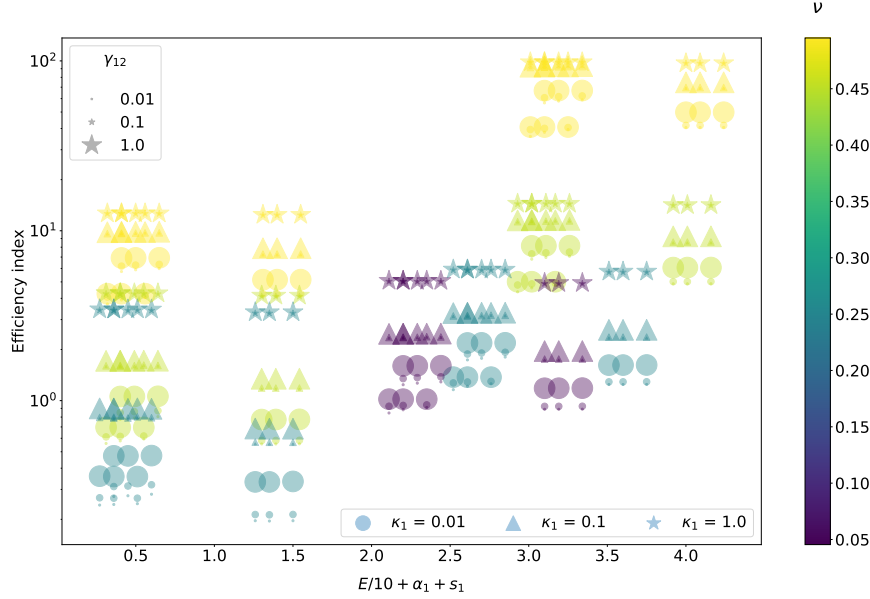


FIGURE 1. Effectivity indices for the smooth 3-network test case for different permutations of material parameters: $\mu \in \{1.0, 10.0, 100.0, 1000.0\}$, $\lambda \in \{1.0, 10.0, 100.0, 1000.0, 10000.0\}$, $\alpha_1 \in \{0.01, 0.1, 0.25\}$ with $\alpha_2 = 0.5 - \alpha_1$, $\alpha_2 = 0.5$, and $s_i, \kappa_i, \gamma_{ij} \in \{0.01, 0.1, 1.0\}$ for $i = 1, 2, 3, j \neq i$. Parameter permutations resulting in $\nu > 0.499$ or $E > 200$ are not visualized. Scatter plot with logarithmic scale on the y-axis, while values on x-axis represent $\alpha_1 + s_1 + E/10$. The color represents ν , the size of the markers represents γ_{12} , and the marker symbol represents κ_1 . Numerical resolution parameters were kept fixed ($T = 0.4$, $\tau = 0.1$, $n = 8$).

7. ADAPTIVE STRATEGY: ALGORITHMIC CONSIDERATIONS AND NUMERICAL EVALUATION

We now turn to consider and evaluate two components of an overall adaptive strategy: (i) temporal adaptivity (only) and (ii) (temporal and) spatial adaptivity with fixed meshes over $[0, T]$. Our choices for the adaptive strategy can be viewed in light of the observations on the convergence of $\eta_1, \eta_2, \eta_3, \eta_4$ for the previous test case, as well as the following characteristics of MPET problems arising in e.g. biological applications:

- Mathematical models of living tissue are often associated with a wide range of uncertainty e.g. in terms of modelling assumptions, material parameters, and data fidelity. Simulations are therefore often not constrained by a precise numerical error tolerance, but rather by the limited availability of computational resources.
- Living tissue often feature heterogeneous material parameters, but typically with small jumps, and in particular smoother variations than e.g. in the geosciences. The corresponding MPET solutions are often relatively smooth.
- Even for problems with a small number of networks J such as single or two-network settings, the linear systems to be solved at each time step are relatively large already for moderately coarse meshes.

In light of these points, our target is an adaptive algorithm robustly reducing the error(s) given limited computational resources. We therefore consider an *error balancing strategy* in which we adaptively refine time steps such that the estimated temporal and spatial contributions to the error is balanced and then refining the spatial mesh to reduce the overall error, and repeat. The

use of a fixed mesh throughout each time evolution can reduce assembly time as the blocks of the MPET linear operator can be reused after updated weighting with the time steps τ_n . We note though that there is ample room for more sophisticated time step control methods than we consider here, see e.g. [Söderlind, 2002] and related works, as well as full time-space adaptivity with meshes varying between time steps, see e.g. [Ahmed et al., 2019, Bendahmane et al., 2010].

7.1. Time adaptivity. We consider the time-adaptive scheme listed in Algorithm 1. Overall, for a given mesh \mathcal{T}_h , we step forward in time, evaluate (an approximation to) the error estimators at the current time step, compare the spatial and temporal contributions to the error estimators, and coarsen (or refine) the time step if the spatial (or temporal) error dominates.

Algorithm 1 Time-adaptive algorithm

- 1: Define adaptive parameters $\alpha \in (0, 1)$ and $\beta \geq 1$, $\tau_{\max} > 0$ and $\tau_{\min} \geq 0$.
 - 2: Assume that a mesh \mathcal{T}_h and an initial time step size τ_0 is given. Set t^0 and set the time step iterator $n = 0$.
 - 3: **while** $t^n < T$ **do**
 - 4: **while** True **do**
 - 5: Set $n = n + 1$.
 - 6: Set $t^* = t^{n-1} + \tau_n$, and solve (4.2) over \mathcal{T}_h for (u_h^*, p_h^*) with time step size τ_n
 - 7: Compute error estimator approximations at the current time step

$$\eta_1^n = (\tau_n \eta_p^n)^{\frac{1}{2}}, \quad \eta_2^n = \left(\sup_{0 \leq m \leq n} \eta_u^m \right)^{\frac{1}{2}}, \quad \eta_3^n = \tau_n (\eta_u^n(\delta_t))^{\frac{1}{2}}, \quad \eta_4^n = (\tau_n \|p_h^n - p_h^{n-1}\|_d^2)^{\frac{1}{2}},$$
 - 8: and set $\eta_h^n = \eta_1^n + \eta_2^n + \eta_3^n$, $\eta_\tau^n = \eta_4^n$.
 - 9: **if** $\eta_\tau^n \leq (1 - \alpha)\eta_h^n$ and $\beta\tau_n \leq \tau_{\max}$ **then**
 - 10: Set $t^n = t^*$, $(u_h^n, p_h^n) = (u_h^*, p_h^*)$, coarsen the next $\tau^{n+1} = \beta\tau^n$, and break loop.
 - 11: **else if** $\eta_\tau^n \geq (1 + \alpha)\eta_h^n$ and $\tau_n/\beta \geq \tau_{\min}$ **then**
 - 12: Discard the solution and refine the time step: set $t^n = t^{n-1}$, $n = n - 1$, $\tau^n = \tau^n/\beta$.
 - 13: **else**
 - 14: Set $t^n = t^*$, $(u_h^n, p_h^n) = (u_h^*, p_h^*)$, $\tau^{n+1} = \tau^n$, and break loop.
 - 15: **end if**
 - 16: **end while**
 - 17: **end while**
-

Evaluation of the time-adaptive algorithm on a smooth numerical test case. We evaluate Algorithm 1 using the numerical test case with smooth solutions defined over 3 networks as introduced in Section 6, the default material parameters, and different uniform meshes (defined by $2 \times N \times N$ triangles as before). We also verified the adaptive solver by comparing the solutions at each time step and error estimators resulting from rejected coarsening and refinement (resulting in $\tau_n = 0.2$ for each n) with the solutions and error estimators computed with a uniform time step ($\tau = 0.2$). We let $T = 1.0$, and considered an initial time step of $\tau_0 = 0.2$, adaptive weight $\alpha = 0$, a coarsening/refinement factor $\beta = 2$, and time step bounds $\tau_{\max} = T$ and $\tau_{\min} = 0.0$.

The discrete times t^n resulting from the adaptive algorithm, error estimators η_h^n and η_τ^n are shown in Figure 2 for different uniform mesh resolutions. For $N = 8$ (Figure 2a), we observe that the adaptive algorithm estimates the initial time step of 0.2 to be unnecessarily small in light of the dominating spatial error, and coarsens the time step to 0.4 before quickly reaching the end of time (T). The $\|u - u_{h\tau}\|_{L^\infty}$, $\|p - p_{h\tau}\|_{L^\infty}$, and $\|p - p_{h\tau}\|_{L^2}$ errors are 4.61×10^{-3} , 3.86×10^{-2} and 6.83×10^{-1} . For comparison, with a uniform time step $\tau = 0.2$, the $\|u - u_{h\tau}\|_{L^\infty}$, $\|p - p_{h\tau}\|_{L^\infty}$, $\|p - p_{h\tau}\|_{L^2}$, and $\|p - \pi^0 p_{h\tau}\|_{L^2}$ (as listed in Table 1) are 4.71×10^{-3} , 4.38×10^{-2} , 4.96×10^{-1} , and 1.33 respectively, and thus the errors with the adaptively defined coarser time step are very comparable - as targeted by our error balancing principle. The picture changes for $N = 16$ (Figure 2b), in this case the temporal error initially dominates the spatial error, and the time step is reduced substantially initially before a subsequent increase and plateau at 0.1 – 0.2. The value of the adaptive error estimator η_4 is lower than for the uniform solution

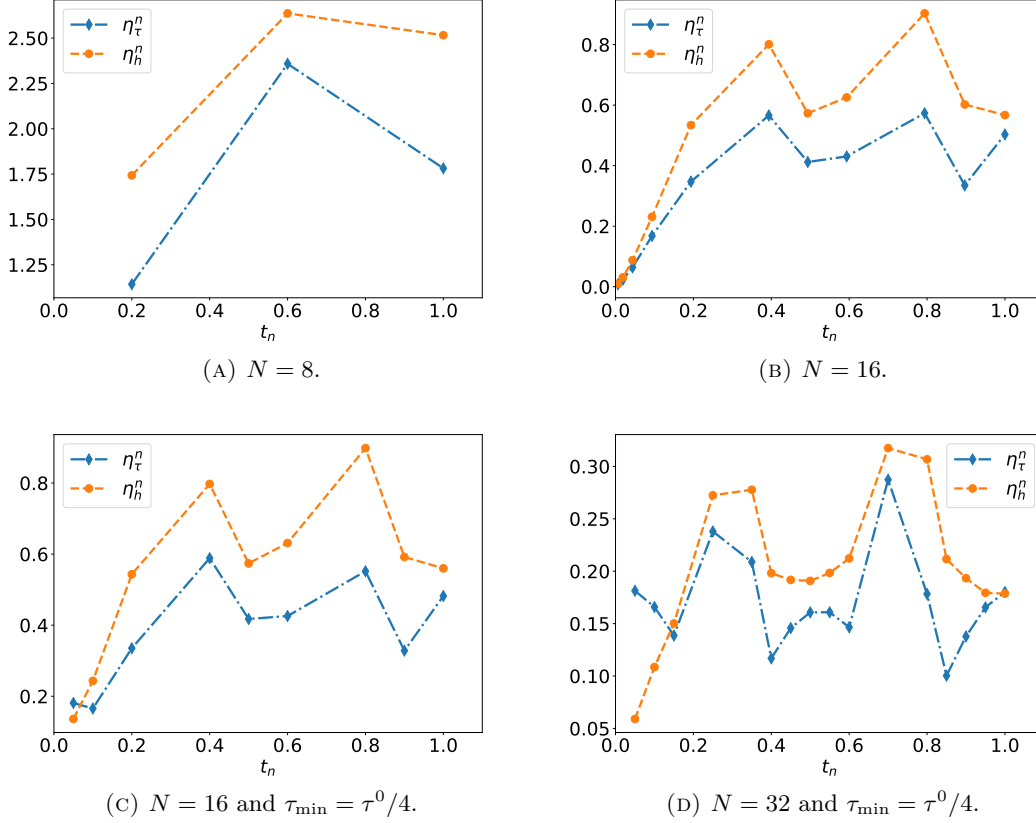


FIGURE 2. Evaluation of adaptive time stepping for a smooth numerical test case, given uniform meshes and different adaptive parameter configurations. All plots show the approximated error estimators η_h^n and η_τ^n at each time step versus adaptive times t^n .

(1.23 vs 2.17), but the exact errors are comparable between the uniform and adaptive scheme in this case. By setting $\tau_{\min} = \tau^0/4$, the unnecessarily high initial time step refinement is limited (Figure 2c), and again comparable errors as for the uniform time step are observed. For higher spatial resolution and thus lower spatial errors ($N = 32$), similar observations hold (Figure 2d), but now the adaptive solutions approximately halve the exact errors compared to the uniform $\tau^0 = 0.2$ case (as expected). We conclude that the time adaptive scheme efficiently balances the temporal and spatial error, but does little for reducing the overall error – as the spatial error dominates this case. For $N = 64$ and the same configurations, the adaptive time step reduces to the minimal threshold $\tau_0/4 = 0.05$ and remains there until end of time T , with the expected quartering of the exact errors compared to the $\tau_0 = 0.2$ case (and the first order accuracy of the temporal discretization scheme).

7.2. Spatial adaptivity. For the spatial adaptivity, we use adaptive mesh (h-)refinement based on local error indicators $\{\eta_K\}_{K \in \mathcal{T}_h}$ derived from the global error estimators (5.20). In light of the theoretical and empirical observation that η_4 primarily contributes to the temporal error, we will rely on local contributions to η_1, η_2 and η_3 only for the local error indicators. Specifically, we will let

$$(7.1) \quad \eta_K = \eta_{1,K} + \eta_{2,K} + \eta_{3,K}$$

where

$$(7.2) \quad \eta_{1,K} = \left(\sum_{n=1}^N \tau_n \eta_{p,K}^n \right)^{\frac{1}{2}}, \quad \eta_{2,K} = \left(\sup_{0 \leq n \leq N} \eta_{u,K}^n \right)^{\frac{1}{2}}, \quad \eta_{3,K} = \sum_{n=1}^N \tau_n \left(\eta_{u,K}^n(\delta_t) \right)^{\frac{1}{2}}.$$

for each $K \in \mathcal{T}_h$. The complete space-time adaptive algorithm is given in Algorithm 2. We here choose to use Dörfler marking [Dörfler, 1996] or a maximal marking strategy in which the γ_M of the total number of cells with the largest error indicators are marked for refinement, but other marking strategies could of course also be used.

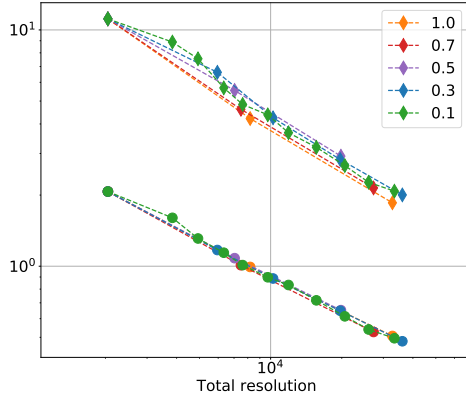
Algorithm 2 Space-time adaptive algorithm

- 1: Assume that an error tolerance ϵ and/or a resource limit L and an initial mesh $\mathcal{T} = \mathcal{T}_h^0$ are given. Set a marking fraction parameter $\gamma_M \in (0, 1]$.
 - 2: **while** True **do**
 - 3: Set the parameters $(\tau_0, \alpha, \beta, \tau_{\max}, \tau_{\min})$ required by Algorithm 1.
 - 4: Solve (4.2) over \mathcal{T} via the time-adaptive scheme defined by Algorithm 1.
 - 5: Estimate the error $\eta = \eta_1 + \eta_2 + \eta_3 + \eta_4$ where η_i for $i = 1, 2, 3, 4$ are given by (5.20).
 - 6: **if** $\eta < \epsilon$ **then**
 - 7: Break
 - 8: **end if**
 - 9: Compute spatial error estimators η_K for $K \in \mathcal{T}$ via (7.1).
 - 10: From $\{\eta_K\}$, define Boolean refinement markers $\{y_K\}_{K \in \mathcal{T}_h}$ via Dörfler or maximal marking (with γ_M).
 - 11: Refine \mathcal{T} (locally) based on the markers $\{y_K\}$.
 - 12: **if** $|\mathcal{T}| > L$ **then**
 - 13: Break
 - 14: **end if**
 - 15: **end while**
-

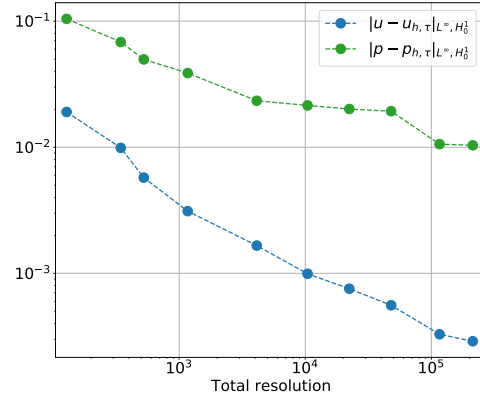
Evaluation of the space-time-adaptive algorithm on a smooth numerical test case. We evaluate Algorithm 2 using the numerical test case with smooth solutions defined over 3 networks as introduced in Section 6 with the default material parameters. As this is a smooth test case in a regular domain, we expect only moderate efficiency improvements (if any) from adaptive mesh refinement, and therefore primarily evaluate the accuracy of the error estimators on adaptively refined meshes and the balance between temporal and spatial adaptivity.

We set $T = 1.0$, $\tau_0 = 0.5$, and begin with a $2 \times 4 \times 4$ mesh of the unit square as \mathcal{T}_h^0 . We set $\epsilon = 0$, but instead prescribe a resource tolerance $L =$. We first set a fine initial time step $\tau_0 = T/64$, and let $\beta = 2.0$, $\alpha = 0.3$, $\tau_{\min} = \tau_0/16$, and $\tau_{\max} = \tau_0$ in Algorithm 1. We note that a Dörfler marking fraction γ_M of 1.0 yields a series of uniformly refined meshes. For marking fractions between 0.0 and 1.0, we obtain adaptively refined meshes, yet for this test case, the time step remains uniform throughout the adaptive loop. The resulting errors and error estimates at each adaptive refinement iteration are shown in Figure 3a. We observe that the errors decay as expected, and that the error estimates provide upper bounds for the errors E at each refinement level for all marking fractions tested.

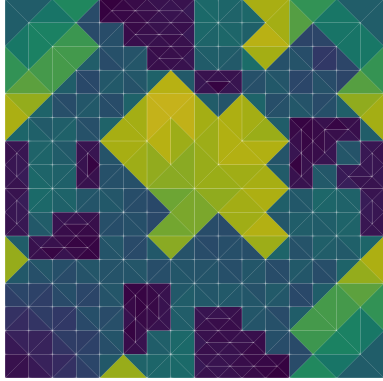
We next let $\tau_0 = T/4$ and $\gamma_M = 0.3$ (and all other parameters as before), and consider the results of the adaptive algorithm (Figure 3b–3d). We find that the adaptive algorithm keeps the initial time step and refines the mesh only for the first 4 iterations, which substantially the $L^\infty H_0^1$ displacement approximation error and moderately reduces the $L^\infty H_0^1$ pressure approximation error. For the next iterations, both the mesh and the time step is refined. The pressure errors seem to plateau before continuing to reduce given sufficient mesh refinement, while the displacement errors steadily decrease.



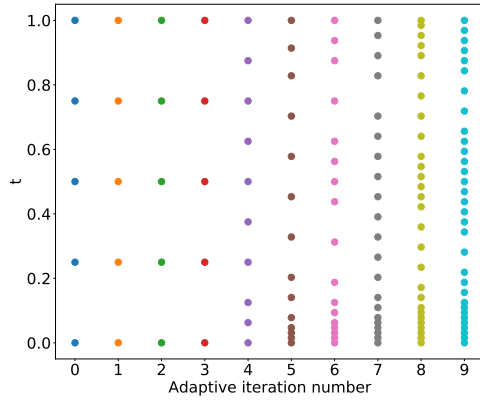
(A) Approximation error E (dots) and error estimates η (diamonds) versus total resolution ($|\mathcal{T}| \times N$) at different adaptive iterations with a uniform timestep $\tau = 1/64$ for different Dörfler marking fractions (1.0, 0.7, 0.5, 0.3, 0.1).



(B) Displacement and pressure approximation errors under adaptive refinement as generated by the space-time adaptive algorithm with $\tau_0 = T/4$, $\alpha = 0.3$, $\beta = 2.0$, $\gamma_M = 0.3$, $\tau_{\max} = \tau_0$, $\tau_{\min} = \tau_0/16$, and $L \approx 8000$.



(C) Error indicators on final mesh refinement level with yellow values indicating high error indicators (colormap: viridis) (same parameters as in Figure 3b).



(D) Discrete times (and time steps) generated by the space-time adaptive algorithm (same parameters as in Figure 3b).

FIGURE 3. Evaluation of the space-time adaptive algorithm on a smooth test case.

8. ADAPTIVE BRAIN MODELLING AND SIMULATION

We turn to consider a physiologically and computationally realistic scenario for simulating the poroelastic response of the human brain. Human brains form highly non-trivial, non-convex domains characterized by narrow gyri and deep sulci, and as such represent a challenge for mesh generation algorithms. Therefore, brain meshes are typically constructed to accurately represent the surface geometry, without particular concern for numerical approximation properties. We therefore ask whether the adaptive algorithm presented here can effectively and without further human intervention improve the numerical approximation of key physiological quantities of interest starting from a moderately coarse initial mesh and initial time step.

Parameter	Value	Note
E (Young's modulus)	1.642×10^3 Pa	[Budday et al., 2015] (gray/white average)
ν (Poisson's ratio)	0.497	*
s_1 (arteriole storage coefficient)	2.9×10^{-4} Pa $^{-1}$	[Guo et al., 2019] (arterial network)
s_2 (venous storage coefficient)	1.5×10^{-5} Pa $^{-1}$	[Guo et al., 2019] (venous network)
s_3 (perivascular storage coefficient)	2.9×10^{-4} Pa $^{-1}$	[Guo et al., 2019] (arterial network)
α_1 (arteriole Biot-Willis parameter)	0.4	*
α_2 (venous Biot-Willis parameter)	0.2	*
α_3 (perivascular Biot-Willis parameter)	0.4	*
κ_1 (arteriole hydraulic conductance)	3.75×10^{-2} mm 2 Pa $^{-1}$ s $^{-1}$	k_1/μ_1 , see below
κ_2 (venous hydraulic conductance)	3.75×10^{-2} mm 2 Pa $^{-1}$ s $^{-1}$	k_2/μ_1 , see below
κ_3 (perivascular hydraulic conductance)	1.43×10^{-1} mm 2 Pa $^{-1}$ s $^{-1}$	k_3/μ_3 , see below
γ_{12} (arteriole-venous transfer)	1.0×10^{-3} Pa $^{-1}$ s $^{-1}$	*
γ_{13} (arteriole-perivascular transfer)	1.0×10^{-4} Pa $^{-1}$ s $^{-1}$	*
C (environment compliance)	10	*
R (environment resistance)	79.8 Pa / (mm 3 / s)	[Vinje et al., 2020]
k_1 (arteriole permeability)	1.0×10^{-10} m 2	[Guo et al., 2019] (arterial network)
k_2 (venous permeability)	1.0×10^{-10} m 2	[Guo et al., 2019] (venous network)
k_3 (perivascular permeability)	1.0×10^{-10} m 2	Estimate, vascular permeability
μ_1 (blood dynamic viscosity)	2.67×10^{-3} Pa s	[Guo et al., 2019] (arterial network)
μ_3 (CSF dynamic viscosity)	6.97×10^{-4} Pa s	[Daverson-Catty et al., 2020] (water at body temperature)

TABLE 3. Material parameters corresponding to a human brain at body temperature. The hydraulic conductances κ are defined in terms of the permeabilities and the fluid viscosities $\kappa_j = k_j/\mu_j$, $\mu_2 = \mu_1$. Values marked by the * are estimates, yielding physiologically reasonable brain displacements, fluid pressures, and fluid velocities.

Specifically, we let Ω be defined by a subject-specific left brain hemisphere mesh (Figure 4a) generated from MRI-data via FreeSurfer [Fischl, 2012] and SVMTK as described e.g. in [Mardal et al., 2021]. The domain boundary is partitioned in two main parts: the semi-inner boundary enclosing the left lateral ventricle $\partial\Omega_v$ and the remaining boundary $\partial\Omega_s$ (Figure 4b).

Over this domain, we consider the MPET equations (3.3) with $J = 3$ fluid networks representing an arteriole/capillary network ($j = 1$), a low-pressure venous network ($j = 2$), and a perivascular space network ($j = 3$). We assume that the two first networks are filled with blood, while the third network is filled with cerebrospinal fluid (CSF). We consider a scenario in which fluid influx is represented by a pulsatile uniform source in the arteriole/capillary network ($j = 1$):

$$(8.1) \quad g_1(x, t) = g_1(t) = \frac{1}{2}(1 - \cos(2\pi t)),$$

while we set $g_2 = g_3 = f = 0$. From the arteriole/capillary network, fluid can transfer either into the venous network or into the perivascular network with rates $\gamma_{12}, \gamma_{13} > 0$, while $\gamma_{23} = 0$. All material parameters are given in Table 3.

In terms of boundary conditions for the momentum equation, we set

$$(8.2a) \quad u = 0 \quad \text{on the outer boundary } \partial\Omega_s,$$

$$(8.2b) \quad (\sigma - \sum_j \alpha_j p_j I) \cdot n = -p_{\text{csf}} n \quad \text{on the inner boundary } \partial\Omega_v.$$

for a spatially-constant p_{csf} to be defined below. For the arteriole space, we assume no boundary flux:

$$(8.3) \quad \nabla p_1 \cdot n = 0 \quad \text{on } \partial\Omega.$$

	#cells	h_{\min}	h_{\max}	#dofs	dV	ΔdV	$\max p_1$	Δp_1	$\max v_2$	Δv_2
a1	20911	1.9	13.8	135774	961	577	1086	541	1.84	0.99
a2	66849	0.86	12.8	364416	1099	643	1144	555	2.08	1.10
a3	198471	0.43	11.4	1021749	1186	677	1177	564	2.28	1.19
u2	167288	0.7	9.8	922350	1162	668	1160	559	2.24	1.18

(A) Quantities of interest on the initial mesh (a1) and two adaptive refinement levels (a2, a3) and after uniform refinement (u2). Each row gives the number of mesh cells (#cells), minimal and maximal cell size h_{\min} , h_{\max} (mm), the number of degrees of freedom per time step (#dofs), the computed peak volume change of the domain dV (mm³), and pulsatile volume change amplitude ΔdV (mm³), peak arteriole/capillary pressure $\max p_1$ (Pa) and its pulsatile amplitude Δp_1 (Pa), peak venous fluid velocity $\max v_2$ (mm/s) and its pulsatile amplitude Δv_2 (mm/s).

	η_1	η_2	η_3	η_4	η
a1	5.6×10^3	5.7×10^5	1.6×10^6	2.9×10^3	2.2×10^6
a2	4.6×10^3	2.7×10^5	7.8×10^5	2.9×10^3	1.1×10^6
a3	3.5×10^3	1.3×10^5	3.9×10^5	2.9×10^3	5.0×10^5

(B) Computed error estimate η and its partial contributions $\eta_1, \eta_2, \eta_3, \eta_4$ (see cf. (5.20)) for the series of adaptively refined brain meshes (a1, a2, a3).

TABLE 4

We assume that the venous network is connected to a low (zero) pressure compartment and set:

$$(8.4) \quad p_2 = 0 \quad \text{on } \partial\Omega.$$

We assume that the perivascular space is in direct contact with its environment, and set:

$$(8.5) \quad p_3 = p_{\text{csf}} \quad \text{on } \partial\Omega.$$

Last, we model p_{csf} via a simple Windkessel model at the boundary:

$$(8.6) \quad C\dot{p}_{\text{csf}} = Q - \frac{p_{\text{csf}}}{R}$$

with compliance C and a resistance R (see Table 3), and where Q is the outflow: $Q = \int_{\partial\Omega} u \cdot n \, ds$. After an explicit time discretization, we define at each time step

$$(8.7) \quad Cp_{\text{csf}}^{n+1} = \tau_n Q^n + (C - \frac{\tau_n}{R})p_{\text{csf}}^n,$$

and use (8.7) in (8.2) and (8.5). Finally, we let all fields start at zero. We let $T = 2.0$ corresponding to two cardiac cycles, and an initial timestep of $\tau_0 = 0.1$.

The given fluid influx induces pulsatile tissue displacements and pressures in the different networks with varying temporal and spatial patterns (Figure 4c, Figure 5). The brain hemisphere expands and contracts with peak changes in volume

$$dV = \int_{\Omega} \text{div } u \, dx,$$

of up to 1200 mm³. The largest displacements occur around the lateral ventricle with peak displacement magnitudes of ≈ 0.5 mm. The arteriole/capillary pressure varies in space and time with a peak pressure $\max p_1$ of up to 1200 Pa, a pressure pulse amplitude Δp_1 of ≈ 560 Pa and a pressure difference in space of ≈ 400 Pa. The venous pressure field show similar patterns, though with lower temporal variations and higher spatial variability inducing higher venous blood velocities of above 2.0 mm/s (Figure 5). The perivascular pressure shows a steady increase of up to ≈ 200 Pa at $T = 2.0$, but only moderate pulsatility and lower fluid velocities than both the arteriole/capillary and venous networks.

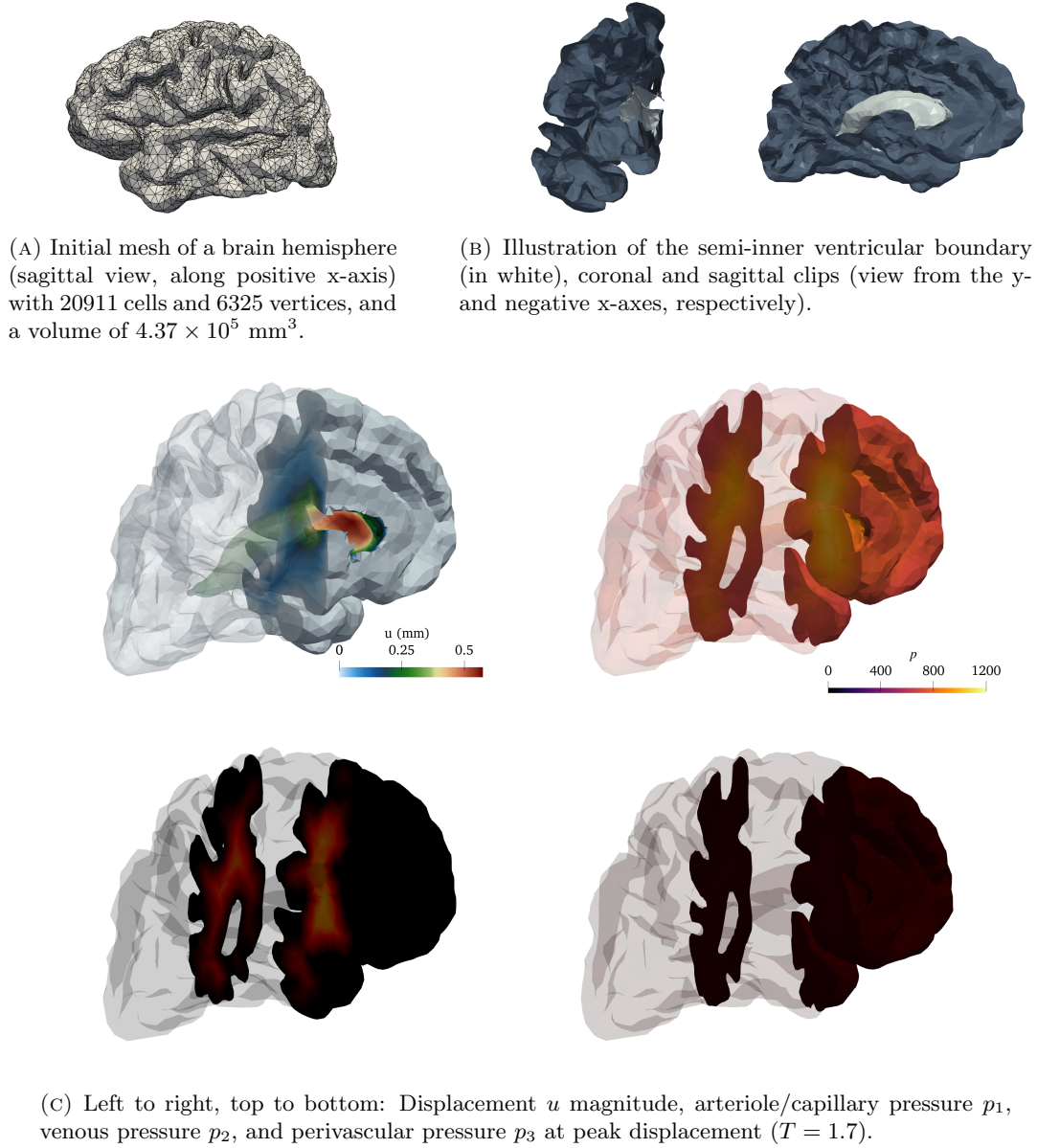


FIGURE 4. The human brain as a poroelastic medium: meshes, boundaries, and snapshots of solution fields.

The local error indicators $\{\eta_K\}_K$ as defined by (7.1) show substantial local error contributions with substantial spatial variation (Figure 6): the values range from the order of 10^3 to 10^9 on the initial mesh \mathcal{T}_h^0 . This large variation in error indicator magnitude makes the choice of marking strategy important: the Dörfler marking strategy would lead to the marking of perhaps only a handful of cells in this case as the local error indicators for a few cells would easily add up to a significant percentage of the total error. Therefore, we instead choose to employ a maximal marking strategy with a marking fraction $\gamma_M = 0.03$ for this test scenario.

The adaptive algorithm yields locally refined meshes with around 67 000 cells after one refinement and 198 000 cells after two. In comparison, a single uniform refinement yields a mesh with around 167 000 cells (Table 4a). We note that the mesh size increase in each adaptive iteration is substantial, even with the small marking fraction of 3%. This behaviour is a consequence of the

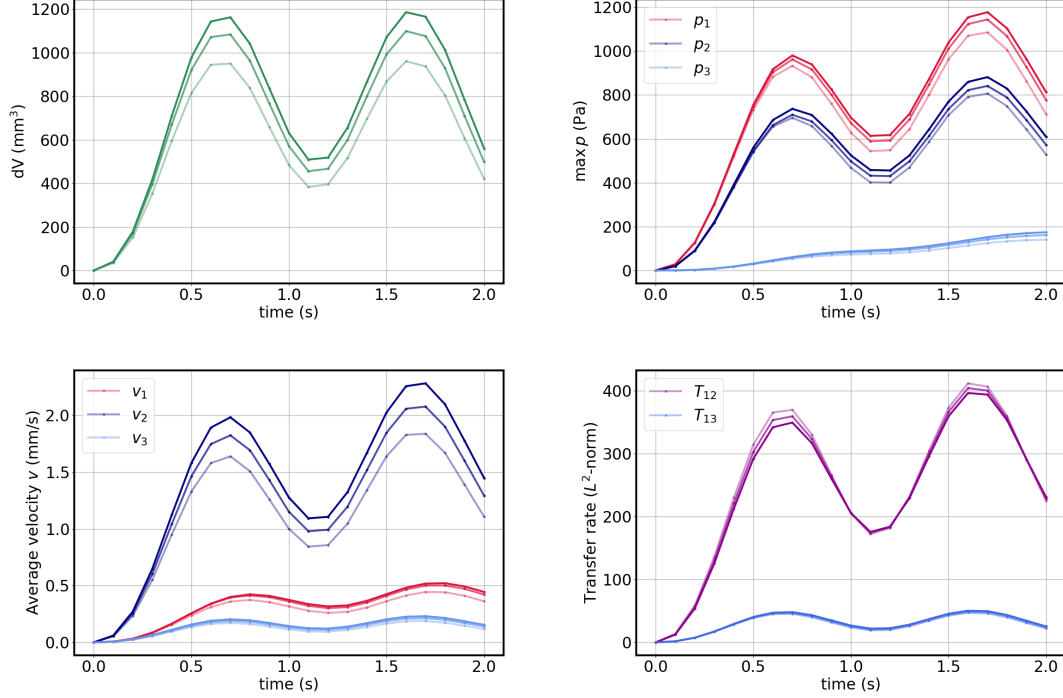


FIGURE 5. Left to right, top to bottom: Volume change dV , peak pressure p_i and average velocity v_i for $i = 1, 2, 3$ and integrated transfer rates T_{12} and T_{13} over time for a series of adaptively refined meshes (a1, a2, a3). The opacity indicates the adaptive level: the more opaque, the finer the mesh.

Plaza refinement algorithm used, and likely of the high domain curvature. More gradual refinement could be perhaps achieved with even lower marking fractions, other refinement algorithms or meshes with hanging nodes. We further observe that the error estimates cf. (5.20) decrease with the adaptive refinement (Table 4b). The contribution from η_2 and η_3 dominates the error estimate, and both of these as well as the total error estimate η seem to halven for each adaptive refinement level. We also note that in this simulation scenario, for all time steps n and refinement levels, the spatial error contribution η_h^n dominates the temporal contribution η_τ^n cf. Algorithm 1. Thus, the adaptive algorithm does not refine the time step and the uniform initial time step of $\Delta t = 0.1$ is kept throughout.

We finally inspect the computed quantities of physiological interest (Table 4a). Using the uniform refinement as an intermediate reference value, we observe that the adaptive algorithm seems to produce more accurate estimates of these quantities of interest even after a single adaptive refinement, and that the quantities of interest after two refinements are more accurate than those of a uniform refinement. The adaptive procedure is therefore able to drive more accurate computation of quantities of interest at a lower or comparable cost as uniform refinement.

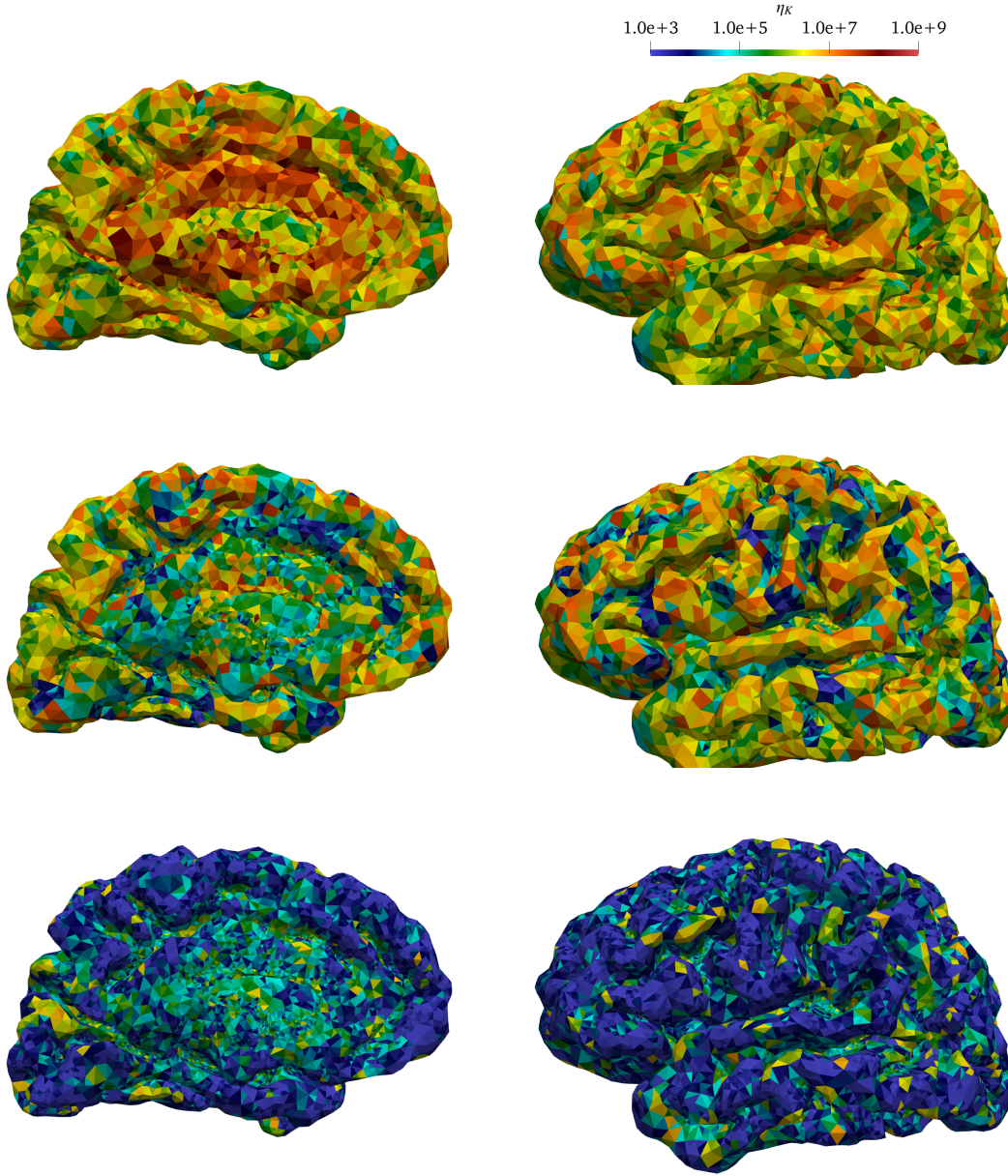


FIGURE 6. Error indicators $\{\eta_K\}_K$ for three levels of adaptive refinement $\mathcal{T}_h^0, \mathcal{T}_h^1, \mathcal{T}_h^2$ the brain simulation scenario. Refinement levels from top to bottom (a1, a2, a3), sagittal views from right and left on the left and right.

ACKNOWLEDGMENTS

We wish to thank Dr. Magne Nordaas and Prof. Ragnar Winther for constructive discussions, as well as Dr. Lars Magnus Valnes for invaluable aid with the human brain mesh generation pipeline.

REFERENCES

- E. Ahmed, F. A. Radu, and J. M. Nordbotten. Adaptive poromechanics computations based on a posteriori error estimates for fully mixed formulations of Biot's consolidation model. *Computer Methods in Applied Mechanics and Engineering*, 347:264–294, 2019.

- E. Aifantis. On the Problem of Diffusion in Solids. *Acta Mechanica*, 37(3-4):265–296, 1980.
- M. Alnæs, J. Blechta, J. Hake, A. Johansson, B. Kehlet, A. Logg, C. Richardson, J. Ring, M. E. Rognes, and G. N. Wells. The fenics project version 1.5. *Archive of Numerical Software*, 3(100), 2015.
- M. Bai, D. Elsworth, and J.-C. Roegiers. Multiporosity/multipermeability approach to the simulation of naturally fractured reservoirs. *Water Resources Research*, 29(6):1621–1633, 1993.
- G. Barenblatt. On certain boundary-value problems for the equations of seepage of a liquid in fissured rocks. *J. Appl. Math. and Mech.*, 27(2):513–518, 1963.
- G. Barenblatt, I. P. Zheltov, and I. Kochina. Basic concepts in the theory of seepage of homogeneous liquids in fissured rocks (strata). *J. Appl. Math. and Mech.*, 24(5):1286–1303, 1960.
- M. Bendahmane, R. Bürger, and R. Ruiz-Baier. A multiresolution space-time adaptive scheme for the bidomain model in electrocardiology. *Numerical Methods for Partial Differential Equations*, 26(6):1377–1404, 2010.
- M. Biot. General theory of three-dimensional consolidation. *J. Appl. Phys.*, 12(2):155–164, 1941.
- M. Biot. Theory of elasticity and consolidation for a porous anisotropic media. *J. Appl. Phys.*, 26(2):182–185, 1955.
- S. Budday, R. Nay, R. de Rooij, P. Steinmann, T. Wyrobek, T. C. Ovaert, and E. Kuhl. Mechanical properties of gray and white matter brain tissue by indentation. *Journal of the mechanical behavior of biomedical materials*, 46:318–330, 2015.
- J. Conway. *A Course in Functional Analysis*. Springer-Verlag, New York, N.Y., 2nd edition, 1997. ISBN 3540972455.
- C. Daversin-Catty, V. Vinje, K.-A. Mardal, and M. E. Rognes. The mechanisms behind perivascular fluid flow. *Plos one*, 15(12):e0244442, 2020.
- W. Dörfler. A convergent adaptive algorithm for poisson’s equation. *SIAM Journal on Numerical Analysis*, 33(3):1106–1124, 1996.
- A. Ern and J.-L. Guermond. *Theory and Practice of Finite Elements*. Springer-Verlag, 2004.
- A. Ern and S. Meunier. A Posteriori Error Analysis of Euler-Galerkin Approximations to Coupled Elliptic-Parabolic Problems. *M2AN Math. Model. Numer. Anal.*, 43(2):353–375, 2009.
- L. Evans. *Partial differential equations*. American Mathematical Society, Providence, R.I., 2010. ISBN 9780821849743 0821849743.
- B. Fischl. Freesurfer. *Neuroimage*, 62(2):774–781, 2012.
- L. Guo, J. Vardakis, T. Lassila, M. Mitolo, N. Ravikumar, D. Chou, M. Lange, A. Sarrami-Foroushani, B. Tully, Z. Taylor, S. Varma, A. Venneri, A. Frangi, and Y. Ventikos. Subject-specific multi-poroelastic model for exploring the risk factors associated with the early stages of Alzheimer’s disease. *Interface Focus*, (8):1–15, 2018. URL <http://dx.doi.org/10.1098/rsfs.2017.0019>.
- L. Guo, Z. Li, J. Lyu, Y. Mei, J. C. Vardakis, D. Chen, C. Han, X. Lou, and Y. Ventikos. On the validation of a multiple-network poroelastic model using arterial spin labeling mri data. *Frontiers in computational neuroscience*, 13:60, 2019.
- M. Khaled, D. Beskos, and E. Aifantis. On the theory of consolidation with double porosity. 3. a finite-element formulation. *Int. J. Num. Anal. Meth. Geomech.*, (8):101–123, 1984.
- A. Khan and D. J. Silvester. Robust a posteriori error estimation for mixed finite element approximation of linear poroelasticity. *IMA J. Numer. Anal.*, 41(3):2000–2005, 2020.
- K. Kuman, S. Kyas, J. Nordbotten, and S. Repin. Guaranteed and computable error bounds for approximations constructed by an iterative decoupling of the biot problem. *Comput. Math. with Appl.*, 91:122–149, 2021.
- J. J. Lee, E. Piersanti, K.-A. Mardal, and M. E. Rognes. A mixed finite element method for nearly incompressible multiple-network poroelasticity. *SIAM Journal on Scientific Computing*, 41(2):A722–A747, 2019.
- Y. Li and L. T. Zikatanov. Residual-based a posteriori error estimates of mixed methods for a three-field Biot’s consolidation model. *arXiv preprint arXiv:1911.08692*, 2019.
- Z. Lotfian and M. Sivaselvan. Mixed finite element formulation for dynamics of porous media. *Int. J. Numer. Methods. Eng.*, 115:141–171, 2018.

- K.-A. Mardal, M. E. Rognes, T. B. Thompson, and L. M. Valnes. *Mathematical modeling of the human brain: from magnetic resonance images to finite element simulation*. Springer, 2021.
- J. M. Nordbotten, T. Rahman, S. I. Repin, and J. Valdman. A posteriori error estimates for approximate solutions of the barenblatt-biot poroelastic model. *Computational methods in applied mathematics*, 10(3):302–314, 2010.
- O. Ricardo and R. Ruiz-Baier. Locking-free finite element methods for poroelasticity. *SIAM J. Numer. Anal.*, 54(5):2951–2973, 2016.
- R. Riedlbeck, D. Di Pietro, A. Ern, S. Granet, and K. K. Stress and flux reconstructions in Biot’s poro-elasticity problem with application to a posteriori error analysis. *Comput. Math. with Appl.*, 73(7):1593–1610, 2017.
- C. Rodrigo, X. Hu, P. Ohm, J. Adler, F. Gaspar, and L. Zikatanov. New stabilized discretizations for poroelasticity and the Stoke’s equations. *Comput. Methods Appl. Mech. Engrg.*, 341:467–484, 2018.
- R. Showalter. Diffusion in Poro-Elastic Media. *J. of Math. Analysis and App.*, 24(251):310–340, 2000.
- G. Söderlind. Automatic control and adaptive time-stepping. *Numerical Algorithms*, 31(1):281–310, 2002.
- K. Terzaghi. *Theoretical Soil Mechanics*. Wiley, 1943.
- B. Tully and Y. Ventikos. Cerebral water transport using multiple-network poroelastic theory: application to normal pressure hydrocephalus. *J. Fluid. Mech.*, 667:188–215, 2011.
- J. Vardakis, D. Chou, B. Tully, C. Hung, T. Lee, P.-H. Tsui, and Y. Ventikos. Investigating cerebral oedema using poroelasticity. *Med. Eng. and Phy.*, (38):48–57, 2016.
- V. Vinje, A. Eklund, K.-A. Mardal, M. E. Rognes, and K.-H. Støverud. Intracranial pressure elevation alters csf clearance pathways. *Fluids and Barriers of the CNS*, 17(1):1–19, 2020.
- R. Wilson and E. Aifantis. On the theory of consolidation with double porosity. *Int. J. Engrg. Sci.*, 20(9):1009–1035, 1982.
- J. Young, B. Riviere, C. Cox, and K. Uray. A mathematical model of intestinal edema formation. *Math. Medic. and Bio.*, 31(1):1189–1210, 2014.

(E. Eliseussen, e.e.odegaard@medisin.uio.no) INSTITUTE OF BASAL MEDICAL SCIENCES, UNIVERSITY OF OSLO, OSLO, NORWAY

(M. E. Rognes, meg@simula.no) DEPARTMENT OF SCIENTIFIC COMPUTING AND NUMERICAL ANALYSIS, SIMULA RESEARCH LABORATORY, OSLO, NORWAY; DEPARTMENT OF MATHEMATICS, UNIVERSITY OF BERGEN, BERGEN, NORWAY.

(T. B. Thompson, travis.thompson@maths.ox.ac.uk) MATHEMATICAL INSTITUTE, UNIVERSITY OF OXFORD, OXFORD, UK